THE UNIVERSITY of EDINBURGH

Edinburgh Research Explorer

Biomimicking Fiber Platform with Tunable Stiffness to Study Mechanotransduction Reveals Stiffness Enhances Oligodendrocyte Differentiation but Impedes Myelination through YAP-dependent Regulation

Citation for published version:
Ong, W, Marinval, N, Lin, J, Nai, MH, Chong, Y-S, Pinese, C, Sajikumar, S, Lim, CT, Ffrench-Constant, C, Bechler, M & Chew, SY 2020, 'Biomimicking Fiber Platform with Tunable Stiffness to Study Mechanotransduction Reveals Stiffness Enhances Oligodendrocyte Differentiation but Impedes Myelination through YAP-dependent Regulation', *Small*. https://doi.org/10.1002/smll.202003656

Digital Object Identifier (DOI):
10.1002/smll.202003656

Link:
Link to publication record in Edinburgh Research Explorer

Document Version:
Peer reviewed version

Published In:
Small

Publisher Rights Statement:
This is the Author's final peer-reviewed manuscript as accepted for publication.

General rights
Copyright for the publications made accessible via the Edinburgh Research Explorer is retained by the author(s) and / or other copyright owners and it is a condition of accessing these publications that users recognise and abide by the legal requirements associated with these rights.

Take down policy
The University of Edinburgh has made every reasonable effort to ensure that Edinburgh Research Explorer content complies with UK legislation. If you believe that the public display of this file breaches copyright please contact openaccess@ed.ac.uk providing details, and we will remove access to the work immediately and investigate your claim.

OPEN ACCESS

Download date: 04. May. 2023

Biomimicking Fiber Platform with Tunable Stiffness to Study Mechanotransduction Reveals Stiffness Enhances Oligodendrocyte Differentiation but Impedes Myelination through YAP-dependent Regulation

Authors: William Ong[1,2], Nicolas Marinval[1], Junquan Lin[1], Mui Hoon Nai[3], Yee-Song Chong[4,5], Coline Pinese[6], Sreedharan Sajikumar[4,5], Chwee Teck Lim[3,7], Charles ffrench-Constant[8], Marie Bechler[8,9], Sing Yian Chew[1,10,#]

1. School of Chemical and Biomedical Engineering, Nanyang Technological University, Singapore 637459, Singapore
2. NTU Institute for Health Technologies (Health Tech NTU), Interdisciplinary Disciplinary School, Nanyang Technological University, Singapore 637533, Singapore
3. Department of Biomedical Engineering, National University of Singapore, 117583, Singapore
4. Department of Physiology, National University of Singapore, Singapore 117593, Singapore
5. Life Sciences Institute Neurobiology Programme, Centre for Life Sciences, National University of Singapore, Singapore 117456, Singapore
6. Max Mousseron Institute of Biomolecules (IBMM), UMR CNRS 5247, University of Montpellier, ENSCM, Montpellier, France
7. Institute for Health Innovation and Technology (iHealthtech), National University of Singapore, Singapore 117599, Singapore
8. MRC-Centre for Regenerative Medicine, University of Edinburgh, 5 Little France Drive, Edinburgh EH164UU, Edinburgh, UK
9. Department of Cell and Developmental Biology, SUNY Upstate Medical University, 750 East Adams Street, Syracuse, NY 13210, USA
10. Lee Kong Chian School of Medicine, Nanyang Technological University, Singapore 308232, Singapore

[#] Corresponding author at: School of Chemical and Biomedical Engineering, Nanyang Technological University, Singapore 637459, Singapore.

Tel.: +65 6316 8812; fax: +65 6794 7553

E-mail address: sychew@ntu.edu.sg (S. Y. Chew)

Abstract

A key hallmark of many diseases, especially those in the central nervous system (CNS), is the change in tissue stiffness due to inflammation and scarring. However, how such changes in microenvironment affect the regenerative process remains poorly understood. Here, we report a biomimicking fiber platform that provides independent variation of fiber structural and intrinsic stiffness. To demonstrate the functionality of these constructs as a mechanotransduction study platform, we utilized these substrates as artificial axons and independently analysed the effects of axon structural vs. intrinsic stiffness on CNS myelination. While studies have shown that substrate stiffness affects oligodendrocyte differentiation, the effects of mechanical stiffness on the final functional state of oligodendrocyte (i.e. myelination) has not been shown prior to this. Here, we demonstrate that a stiff mechanical microenvironment impedes oligodendrocyte myelination, independently and distinctively from oligodendrocyte differentiation. We identified YAP to be involved in influencing oligodendrocyte myelination through mechanotransduction. The opposing effects on oligodendrocyte differentiation and myelination provide important implications for current work screening for promyelinating drugs, since these efforts have focused mainly on promoting oligodendrocyte differentiation. Thus, our novel platform may have considerable utility as part of a drug discovery programme in identifying molecules that promote both differentiation and myelination.

Introduction

Many cell types are mechanosensitive, responding to different levels of environmental stiffness by altering cell proliferation, migration and/or differentiation. This is particularly relevant for development and regeneration following injury. For example, changes in stiffness help guide axons, and substrates mimicking the stiffness of muscle and bone direct the differentiation of mesenchymal stem cells to appropriate fates[1,2]. Equally, altered physical cues in damaged tissue may hinder the regenerative process. For instance, the soft mechanical signature of scarring in the central nervous system (CNS) is correlated to regenerative failure[3]. Thus, an important question is whether changes in stiffness associated with development or injury contribute to the developmental pattern or decline of regeneration that is seen in most adult tissues, such as in the CNS.

Corresponding to our enhanced awareness of the importance of mechanical signals in modulating cell functionality, diverse platforms have been used to study cell-matrix mechanotransduction. For instance, two-dimensional (2D) hydrogels (e.g. polyacrylamide (PA) [4,5]) and micropillars[6,7] are commonly used. These substrates allow convenient tuning of matrix stiffness either by varying polymer crosslinking density[4,5] or altering the physical dimensions of the micropillars[6,7]. While these powerful platforms have advanced our understanding of cell mechanotransduction, the topography that these systems provide remains distant from the fibrillar architecture that is often observed in the native extracellular matrix (ECM) environment. This major drawback has limited the extent of mechanotransduction studies on the functionality of several cell types, such oligodendrocyte (OL) myelination. Hence, innovative techniques for studying cell mechanotransduction are required.

Oligodendrocytes (OLs), the myelin-forming cells of the CNS, are mechanosensitive. In particular, physical cues have emerged as drivers of oligodendrocyte precursor cell (OPC) behaviour and developmental myelination. In this regard, OPC differentiation is influenced by spatial constraints[8]. As well, the physical cue of diameter has been shown to be sufficient to instruct myelin wrapping and lengthening to physiological lengths[9]. While several studies have indicated stiffness impacts differentiation of OPCs to OLs[10,11], it remains unclear whether environmental stiffness also impacts the final three-dimensional (3D) multilamellar myelination process, which determines the ultimate functionality of OLs.

Here, we devise a novel biomimicking fiber platform for cell mechanotransduction analyses. Using classical structural mechanics principles, this simple but effective construct allows the independent manipulation of various physical parameters (fiber diameter, fiber alignment, fiber density, structural stiffness and intrinsic stiffness) such that the observed mechanotransduction outcomes can be attributed to the intentionally isolated parameter-of-interest. The fiber architecture of our platform not only mimics the ECM topography[12] but may also be expanded to recapitulate the structure of a neuronal axon, hence serving as artificial axons. Using OLs and their precursor cells as a proof-of-principle, we demonstrate that this fiber system could be used to tease apart the involvement of mechanical stiffness in cell fate commitment as oligodendroglial cells change their interactions with the extracellular environment from 2D to 3D, while undergoing changes from OPC differentiation into adult OLs and finally, to the functional state of myelination.

Results

High axon intrinsic stiffness promotes OL differentiation but impedes myelination

We and others have shown that OLs will form myelin sheaths of physiological length on electrospun fibers, which possess diameters that match that of CNS axons[9,13,14]. In these studies, the effects of physical size were examined but not the mechanical properties. To address the possible effects of stiffness on myelination, we generated electrospun fibers of differing stiffness with controlled density by using different polymers – poly(ε-caprolactone) (PCL), poly(lactic acid) (PLA) (Figure 1, Supplementary Figure 1) and gelatin. Hence, we ensured the same fiber density for each polymer of various stiffness, thereby guaranteeing the cells a similar chance of encountering fibers.

Crystallinity differences in PCL and PLA fibers and variations in the extent of gelatin crosslinking could allow engineering of electrospun fibers with various intrinsic stiffnesses (Figure 1a and b). We devised such an approach to mimic possible changes in axon intrinsic stiffness (i.e. how easily an axon can be compressed), which may occur due to changes in axon viscosity[15] and/or cytoskeletal alterations in axons[15-18] as seen in aging[15] and neural diseases[16]. We used atomic force microscopy (AFM) to confirm the variations in stiffness (Figure 1d), and then plated OPCs onto the fibers. We measured differentiation at Day 3 (D3) by the expression of myelin basic protein (MBP) in the cell bodies and myelination at D10 by the presence of sheaths completely surrounding the fibers at the ends of cell processes (Figure 1e-k). The effects of axon intrinsic stiffness variations on cellular behavior were analyzed and compared within the same type of material and not across different materials, so that surface chemistry effects may be ignored. Correspondingly, we observed that with increasing levels of stiffness, the number of cells expressing MBP increased while the number

of cells forming sheaths was reduced, regardless of the chemistry of the material. The myelin sheath formation at Day 10 was not assessed on gelatin fibers. Specifically, we were not able to observe functional myelination of the gelatin-based artificial axons. We believe that the high rate of degradability of gelatin in culture medium in the presence of cells, did not allow a robust and sustained anchoring of oligodendrocytes to support myelin sheath formation.

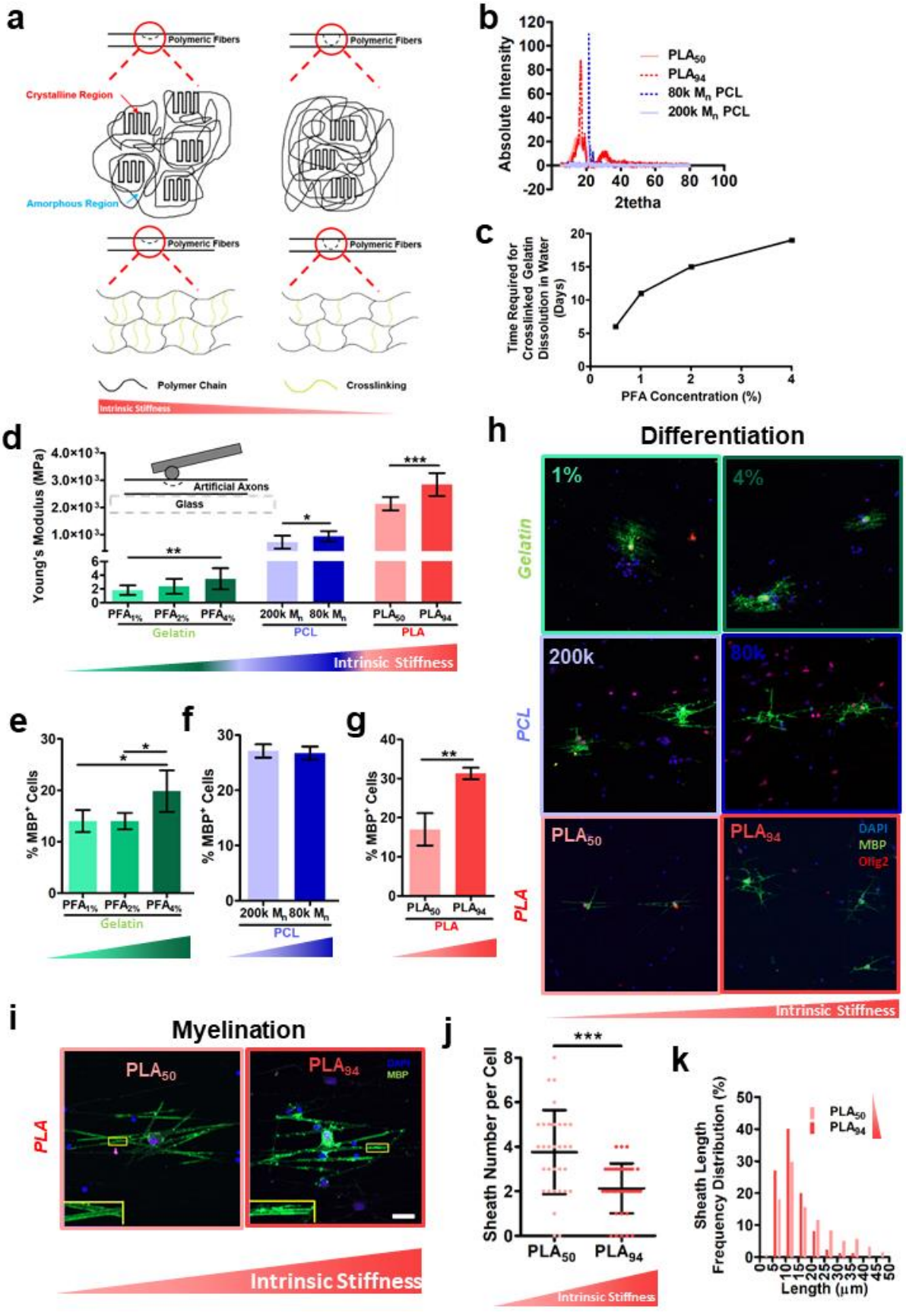
a
Polymeric Fibers
Crystalline Region
Amorphous Region
Polymer Chain
Crosslinking
Intrinsic Stiffness
b
Absolute Intensity
2tetha
PLA50
PLA94
80k Mn PCL
200k Mn PCL
c
Time Required for Crosslinked Gelatin Dissolution in Water (Days)
PFA Concentration (%)
d
Young's Modulus (MPa)
Artificial Axons
Glass
PFA1% PFA2% PFA4%
200k Mn 80k Mn
PLA50 PLA94
Gelatin
PCL
PLA
Intrinsic Stiffness
e
% MBP+ Cells
f
% MBP+ Cells
g
% MBP+ Cells
h
Differentiation
1%
4%
Gelatin
200k
80k
PCL
PLA50
PLA94
DAPI
MBP
Olig2
PLA
Intrinsic Stiffness
i
Myelination
PLA50
PLA94
DAPI
MBP
PLA
Intrinsic Stiffness
j
Sheath Number per Cell
PLA50 PLA94
Intrinsic Stiffness
k
Sheath Length Frequency Distribution (%)
PLA50
PLA94
Length (μm)

Figure 1. High axon intrinsic stiffness impedes OL myelination. (a) Schematic showing principle of tunable axon intrinsic stiffness by altering degree of crystallinity or extent of crosslinking of artificial axons. **(b)** X-ray diffraction patterns supporting enhanced crystallinity of artificial axons as isomer content decreases (PLA94 > PLA50) and polymer molecular weight reduces (80k M_n PCL > 200 k M_n PCL). **(c)** In vitro degradation test supporting enhanced crosslinking of gelatin, which resulted in increased stability of gelatin-based artificial axons. **(d)** AFM results showing variation in intrinsic stiffness of artificial axons by altering degree of crosslinking of (gelatin) or by changing crystallinity of artificial axons (PCL, PLA). *p < 0.05, **p < 0.01, ***p < 0.001, one-way ANOVA with Tukey post-hoc for gelatin samples, independent t-test for PCL and PLA samples. 30 gelatin, 20 PCL and 20 PLA fibers electrospun on a glass substrate were measured. **(e-g)** Quantitative data showing percentage of MBP^+ OLs on artificial axons with various intrinsic stiffness. In gelatin and PLA fibers, high intrinsic stiffness promotes OPC differentiation into OLs. *p < 0.05, **p < 0.001, one-way ANOVA with Tukey post-hoc for gelatin samples, independent t-test for PCL and PLA samples. 3 experimental repeats from cells pooled together from 9 animals. **(h)** Representative confocal images showing increasing OPC differentiation into OLs on artificial axons with high intrinsic stiffness. Scale bar represents 50 μm. **(i)** Confocal images show PLA artificial axons with high intrinsic stiffness hinders OL myelination. Scale bar represents 20 μm. **(j)** Quantitative data shows axon with higher intrinsic stiffness hinders formation of myelin sheath per cell (***p < 0.001, t-test) and results in **(k)** formation of shorter myelin sheaths. 65 cells pooled from 3 independent experiment and 9 animals. All statistical analysis was conducted using n = 3 experimental (biological) repeats.

Structurally compliant axons decrease OL differentiation but promote myelination

While the experiments with varying axon intrinsic stiffness suggest the important conclusion that stiffness has opposing effects on differentiation and myelination, it is also important to realize that in some pathological conditions, e.g. in an MS lesion, it is the environment surrounding the axon, rather than the axon itself, that is likely responsible for changes in stiffness due to extracellular matrix (ECM) deposition. To address this, we extended our experimental model such that the fibers are suspended in a bridge between two supports (Figure 2, Supplementary Figure 2).

Here, the flexibility of the suspended fibers (i.e. structural stiffness) rather than their intrinsic stiffness and surface properties becomes the major determinant of the stiffness detected by the OPCs (Figure 2a & b, Supplementary Figure 3). Moreover, this stiffness can, by altering the length of the bridge, be tuned to differing and lower levels than that possible in the experiments above without changing the fiber topography or calibre (Supplementary Figures 2 and 3). Here again we observed opposing effects of stiffness on differentiation and myelination, with differentiation increasing by 47% as the substrate stiffness was increased from 0.014 N/m to 0.050 N/m while myelin sheath number and length per cell decreased by 5.4 times and 2.3 times respectively (Figure 2b-h). This myelination trend was also observed in two PLA isomers (Supplementary Figure 4).

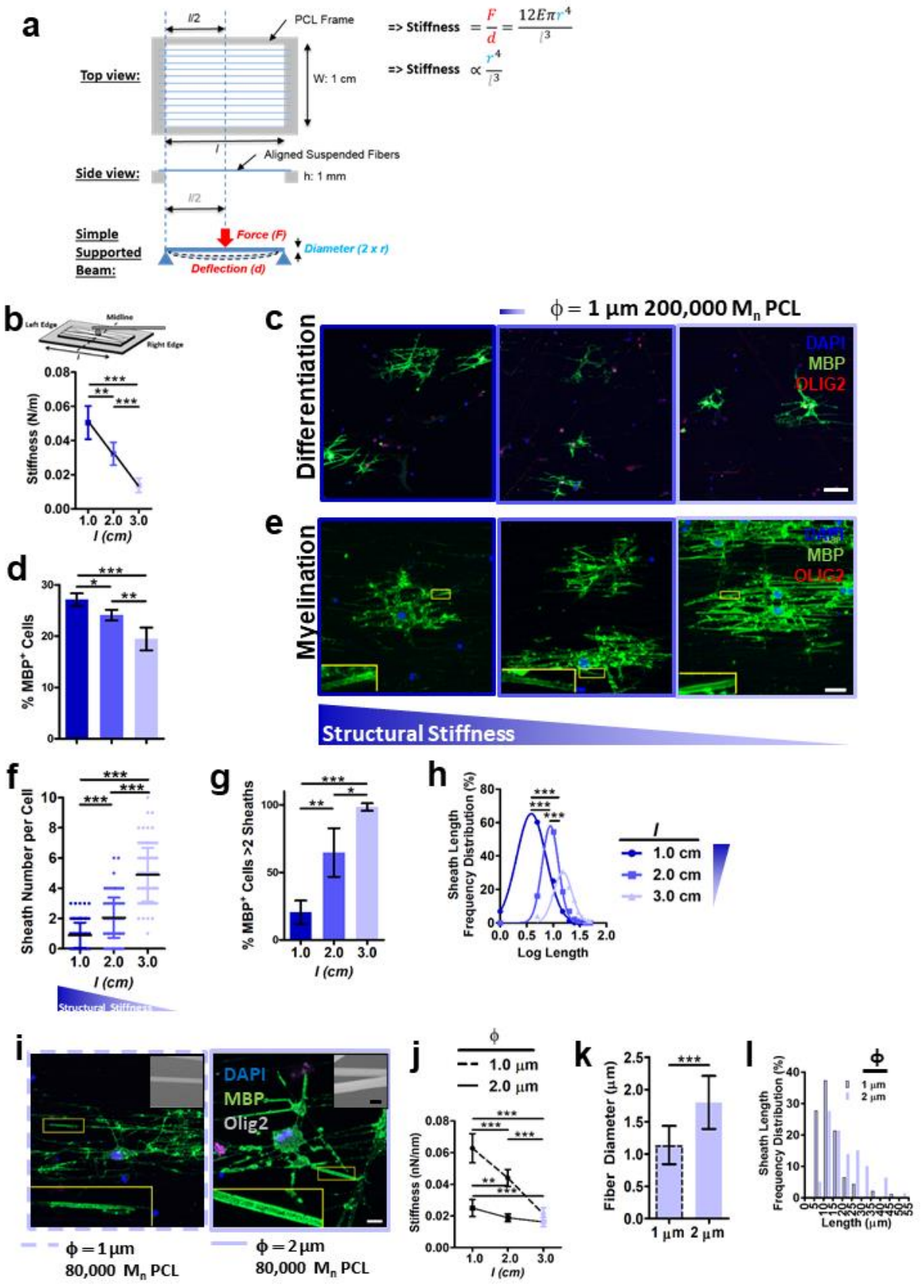
a
l/2
PCL Frame
Top view:
W: 1 cm
l
Aligned Suspended Fibers
Side view:
h: 1 mm
Simple Supported Beam:
Force (F)
Deflection (d)
Diameter (2 x r)
=> Stiffness = F/d = 12Eπr^4/l^3
=> Stiffness ∝ r^4/l^3
b
Left Edge
Midline
Right Edge
Stiffness (N/m)
l (cm)
c
ϕ = 1 µm 200,000 Mn PCL
Differentiation
DAPI
MBP
OLIG2
e
Myelination
Structural Stiffness
d
% MBP+ Cells
f
Sheath Number per Cell
l (cm)
g
% MBP+ Cells >2 Sheaths
h
Sheath Length Frequency Distribution (%)
Log Length
l
1.0 cm
2.0 cm
3.0 cm
i
DAPI
MBP
Olig2
ϕ = 1 µm
80,000 Mn PCL
ϕ = 2 µm
80,000 Mn PCL
j
ϕ
1.0 µm
2.0 µm
Stiffness (nN/nm)
k
Fiber Diameter (µm)
1 µm 2 µm
l
Sheath Length Frequency Distribution (%)
Length (µm)

Figure 2. Structurally compliant axons decrease OL differentiation but promote myelination. (a) Schematic showing principle of tunable axon structural stiffness. By assuming each artificial axon as a simple supported beam, structural stiffness along the midline of the supported axon is related to the ratio of axon radius, r, and length of support, ***l***. **(b)** Quantitative AFM data showing decreasing axon structural stiffness with increasing support length, ***l***. **p<0.01, ***p<0.001; One-way ANOVA. 60 points were measured on 3 suspended fiber samples. **(c)** Confocal images showing enhanced OPC differentiation as axon structural stiffness increased. Scale bar represents 50 μm. **(d)** High axon structural stiffness promotes OPC differentiation into MBP^+ OLs. *p < 0.05 **p < 0.01 ***p < 0.001, One-way ANOVA with Tukey post-hoc. 3 experimental repeats from cells pooled together from 9 animals. **(e)** Confocal images showing high axon structural stiffness impedes OL myelination, while structurally soft axons promote myelination. Scale bar represents 20 μm. **(f-h)** High artificial axon structural stiffness impedes myelination by decreasing average myelin sheath per OL, decreasing the percentage of MBP+ cells with at least 2 sheaths and length of myelin extensions on artificial axons. *p<0.05, **p<0.01, ***p < 0.001, One-way ANOVA with Tukey post-hoc. 280 cells pooled from 3 independent experiment and 9 animals. **(i)** Confocal images showing longer myelin sheaths formed on larger diameter axons. Scale bar represents 20 μm. Embeded SEM images of 2 artificial axon platforms (80k M_n PCL, l = 3 cm) with different axon diameter but similar structural stiffness. Scale bar represents 2 μm. **(j-l)** Quantitative results showing larger axon diameter promotes formation of longer myelin sheaths with similar axon structural stiffness, **(j-k)** Quantitative AFM data showing the ability to modulate axon diameter and suspended length l to obtain platforms with similar axon structural stiffness. Samples indicated in blue were used for understanding axon caliber effect on myelination, independent of axon stiffness effects. **p < 0.01, ***p < 0.001, One-way ANOVA with Tukey

post-hoc. (J, L) 144 points were measured on at least 3 independent suspended fiber per sample group. ***p<0.001, Independent t-test. 200 fibers were measured from 5 distinct ROI and 3 different samples. 66 cells pooled from 3 independent experiment and 9 animals. All statistical analysis was conducted using n = 3 experimental (biological) repeats.

OLs react to structural stiffness changes in their immediate vicinity

The design of the fiber bridge system allows two further questions to be addressed. First, is the effect seen on all axon diameters? OLs form longer sheaths on large diameter axons, both *in vivo* and on artificial fibers[9,13], raising the possibility that the enhanced myelination at lower stiffness might be lost as axon diameter changes. However, this was not the case; the opposing effects on differentiation and myelination were seen at both fiber diameters tested (Figure 1g & j, diameter 1.5 μm; Figure 2d & f, diameter 1.0 μm). Moreover, the fiber bridge system reaffirms that axon diameter has an effect when stiffness is constant (Figure 2i-l, Supplementary Figures 1 and 2). Second, is the effect entirely cell intrinsic, or do paracrine effects play a role? To answer this, we took advantage of another property of the bridge – that stiffness will become greater as the flexibility is lost next to the support structure (Figure 3a-e). By comparing cells at the ends of the bridge (near the supporting structure) with those in the middle in a single experiment we showed that the effects on myelination were determined entirely by the stiffness of their immediate environment, and there was no evidence for paracrine effects.

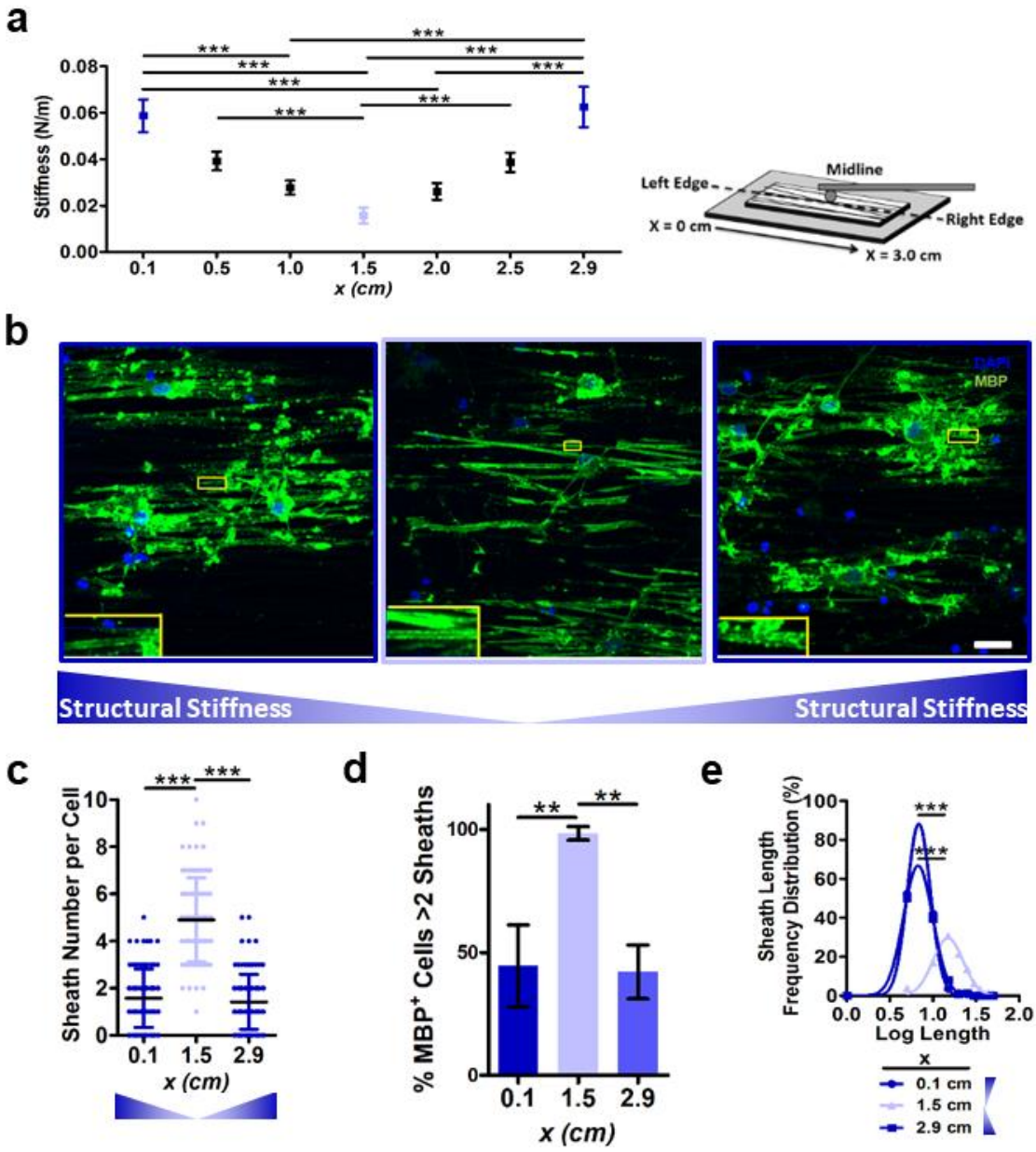

Figure 3. OLs react to structural stiffness changes in their immediate vicinity. (a) AFM data showing lowest structural stiffness at midpoint of platform. ***p < 0.001 One-way ANOVA, with an average of 15 randomly selected points per sample length in 3 distinct set of scaffolds. **(b)** Confocal images showing more complete myelin sheaths and greater sheath length on artificial axons, where structural stiffness was lowest, i.e. along midline of 3.0 cm PCL frame structure. Scale bar represents 20 µm. **(c-e)** Quantitative data showing lower myelin sheath number per OL, lower percentage of MBP+ cells with at least 2 sheaths and shorter average

myelin sheath length at structurally stiff ends vs structurally soft midpoint of artificial axon platform. **p<0.01, one-way ANOVA, ***p < 0.001, Kruskal-Wallis. 276 cells pooled from 3 independent experiment and 9 animals. All statistical analysis was conducted using n = 3 experimental (biological) repeats.

YAP relay mechanotransduction signals in myelinating OLs but not in differentiating OPCs

Previous work on cell intrinsic mechanisms responsive to substrate stiffness have identified the nuclear translocation of YAP as a key step[19]. Also, others have identified YAP to be involved in OL mechanosensing and transiently activated during OL morphogenesis[20,21]. As a proof-of-principle, we investigated the involvement of YAP signalling in OL by using our PCL-based artificial axons to demonstrate the feasibility to study OL mechanotransduction pathways. We used our 3D platform (stiff = 0.050 N/m and compliant = 0.014 N/m) to further explore the YAP implication by decoupling two biological phenomena (OL differentiation and myelination) in a timely fashion. We found that cell immaturity and increasing stiffness was associated with increased levels of nuclear YAP (Figure 4a-c) and also that blocking YAP with verteporfin reduced the anti-myelination effect of stiffer substrates, showing that YAP regulates the mechanotransduction pathway leading to myelination by OLs (Figure 4d-i). There was, however, minimal impact on differentiation (Figure 4j-l), arguing that different mechanosensitive pathways regulate this aspect of OL behaviour.

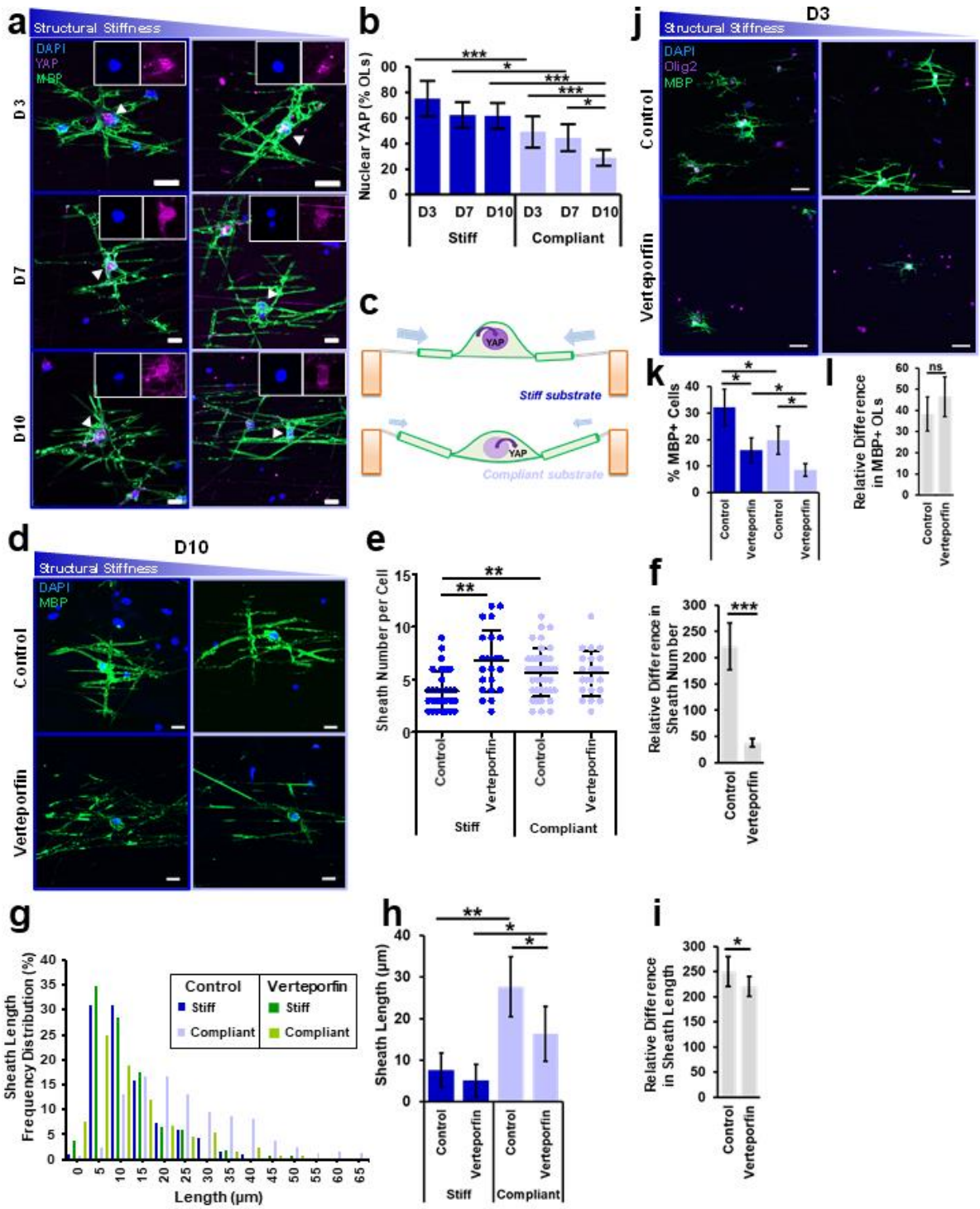

Figure 4. YAP relay mechanotransduction signals in myelinating OLs but not in differentiating OPCs. **(a)** Confocal images show structurally stiff axons (PCL) promoted YAP nuclear translocation throughout OL differentiation (D3-D7) and myelination (D10). Scale bar represent 20 μm. **(b)** Quantitative data show consistent enhanced YAP nuclear translocation on structurally stiff axons throughout OPC differentiation and myelination. *p < 0.05, one-

way ANOVA with Tukey post-hoc test. **(c)** Schematic showing enhanced YAP nuclear translocation on structurally stiff axons. **(d)** Confocal images showing reduced myelination by OLs on structurally stiff artificial axons and a corresponding increase in stiffness-regulated myelination with YAP inactivation by verteporfin (0.1 μM). Scale bar represent 20 μm. **(e-i)** Quantitative data showing YAP inhibition significantly altered axon structural stiffness-mediated OL myelination by changing **(e, f)** number of myelin sheath per cell and **(g-i)** myelin sheath length. (f) and (i) are showing the difference between the compliant and stiff axon relative to the stiff axon [(Compliant – Stiff) / Stiff x 100 %)]. **(j)** Confocal images showing decrease in OPC differentiation into MBP^+ OLs on structurally compliant artificial axons, regardless of YAP inactivation by verteporfin (0.1 μM) Scale bar represent 50 μm. **(k)** Quantitative data showing decrease in OPC differentiation into MBP^+ OLs on structurally compliant artificial axons, regardless of YAP inactivation by verteporfin (0.1 μM). *$p < 0.05$, one-way ANOVA with Tukey post-hoc test. **(l)** Quantitative data showing that verteporfin did not affect the stiffness effect on OPC differentiation into MBP^+ OLs. Data are showing the difference between the compliant and stiff axons relative to the stiff axon [(Compliant – Stiff) / Stiff x 100 %)]. *$p < 0.05$, ** $p < 0.01$, *** $p < 0.001$, one-way ANOVA with Tukey post-hoc test. All statistical analysis was conducted using n = 3 experimental (biological) repeats.

Compliant brain region is associated with high degree of myelination during development

In order to validate the effect of stiffness on myelination, we further sampled live brain slices of rodents with AFM. Specifically, regions with distinct myelination patterns, such as the densely myelinated corpus callosum (CC) and the cortex, which is characterized by sparse myelination (Figure 5a), were investigated. Active myelination in rodent corpus callosum is initiated around 7 days postnatal (P7) and completed by P35[22]. During this period

of development, the cortex remains sparsely myelinated. We observed a consistent trend that the CC, being highly myelinated, was significantly more compliant ($p < 0.001$) than the cortex during peak myelination (P15) and end of active myelination (P35)(Figure 5b). Additionally, we noticed that the increment in stiffness of the cortex decelerated over time while the CC remains relatively compliant throughout the entire active myelination phase. Taken together, our data suggest that environmental stiffness directly impacts myelination.

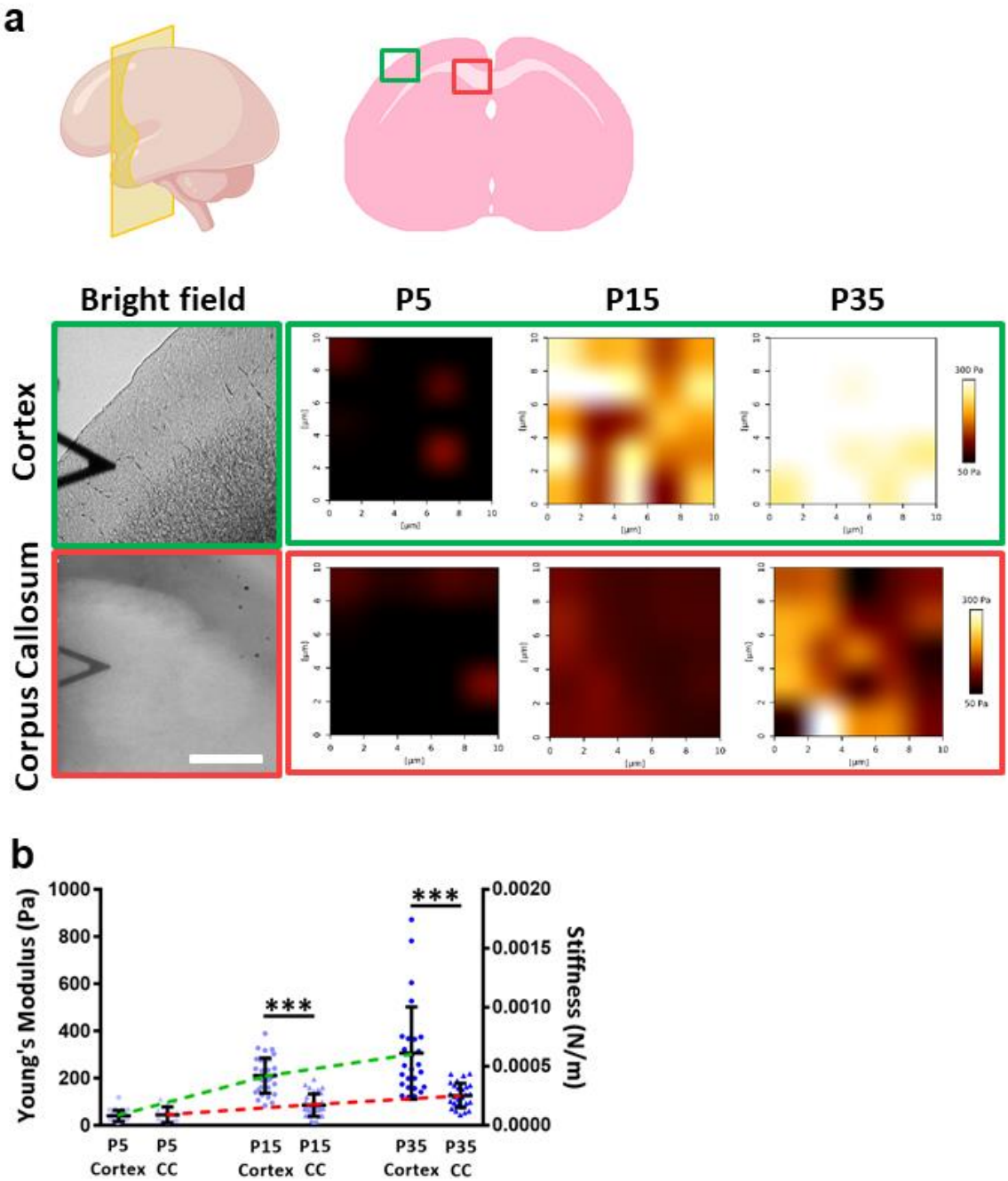

Figure 5. Compliant brain region is associated with high degree of myelination during development. (a) Bright field images showing indentation of cortex and corpus callosum (CC). Scale bar represents 5 µm. Heat map showing AFM measurements of elastic modulus of living rat brain slices at cortex and CC across three time points. Scale bar represents 2 µm. **(b)** Quantitative AFM data showing negligible stiffness differences between the cortex and CC at P5, which corresponds to the developmental stage of rodent where there is no significant myelination. Significantly higher stiffness in the sparsely myelinated cortex than heavily myelinated CC at both P15 and P35, which corresponds to the peak and diminishment of active developmental myelination respectively. $^{**}p < 0.01$, $^{***}p < 0.001$, One-way ANOVA with Tukey post-hoc. 5 regions in every cortex and CC, spanning a 5 x 5 μm^2 area (25 points of indentations) per region, were measured. A total of 2 animals per group (for P5, P15, P35) per experimental repeat, with a total of 3 experimental repeats, were used. All the values were pooled together and displayed in **(b)**. Statistical analysis was conducted by using the average values obtained from each experimental repeat and comparing between the different time points.

Discussion

A major characteristic of many diseases is the change in tissue stiffness because of inflammation and scarring. Unfortunately, our understanding on how these alterations in microenvironmental mechanical stiffness affects tissue regeneration remains insufficient. To enhance our knowledge, innovative experimental platforms and techniques would be required for understanding cell response towards mechanical stimuli. In this work, we designed a reproducible and 3D fiber platform to recapitulate the microenvironment that surrounds cells. In order to demonstrate the feasibility of our platform for studying cell

mechanotransduction, we chose oligodendroglial cells as our model cell type because of their unique cell-ECM interactions that puts additional demands on study platforms to assess their mechanosensing behaviour. On the other hand, the final functional state of myelination takes place in a 3D configuration (i.e. wrapping around axons), which in turn requires a 3D scaffold to support this phenomenon. Here, we showed that our fiber construct could easily fulfil these demanding requirements of scaffold architecture.

Understanding OL behaviour is interesting and important because the effects of stiffness on myelination is also of particular relevance in disease context, such as in the case of multiple sclerosis (MS). In MS, the myelin sheaths that are essential for axon support in the CNS are destroyed by inflammation. A regenerative process known as remyelination occurs early in the course of the disease but eventually fails in many patients, which could cause neurodegeneration[23]. This failure of regeneration is associated with the presence of focal lesions devoid of myelin despite minimal ongoing inflammation – so-called chronic inactive lesions. Promoting remyelination in these lesions is a key goal for ongoing research but at present we have a limited understanding of the mechanism leading to failure in the regenerative process[23].

These lesions, as suggested by the name of the disease, are stiffer than the normal CNS (sclerotic)[24]. The effect that this increased stiffness might have on the generation of OLs from resident OPCs has been addressed in a number of studies[4,20]. These have shown that OPCs are mechanosensitive, with substrate stiffness altering differentiation via signalling through the YAP/TAZ pathway[20]. In addition, we found YAP to be differentially involved in influencing oligodendrocyte differentiation and myelination through mechanotransduction in

the absence of other chemical stimuli. Importantly, increasing tissue stiffness with ageing instructs OPC behaviour by reducing proliferation[4]. However, while these findings are clearly relevant to remyelination failure in the ageing brain, they do not address the effect of stiffness on the key final step in the myelination process – the formation of a multi-layered 3D myelin sheath around the axon. Given the failure of this final step in many MS lesions, as evidenced by the presence of OLs but no remyelination, this is an important omission.

YAP activation is transient and regulated by numerous mechanotransduction factors[19]. During OL maturation, YAP was demonstrated to be involved at the early stages[20], while in Schwann cells, YAP was found crucial for the initiation and maintenance of peripheral myelination[25,26]. This bundle of clues indicates that YAP could also be transiently used by OLs during maturation and myelination. Verteporfin is a potent inhibitor of YAP transcriptional activity with an EC50 at 0.1 μM[27]. We performed verteporfin titration (0.1, 1 and 10 μM, data not shown) in culture medium and selected the optimal concentration (0.1 μM) to target YAP inactivation and limit off target effect that would decrease cell viability. While other studies used verteporfin at higher concentrations (2-10 μM), they only focused on the changes in gene expression in short term (24 h). In our study, we chose to focus on the prolonged inhibition of YAP activity to observe the involvement of YAP in a timely fashion on the OL differentiation and myelination as assessed on the various axon stiffnesses. While verteporfin has been widely used to elucidate the involvement of YAP in cell mechanotransduction[25,28,29], its mode of inhibition and mechanism of interaction with YAP remain largely to be elucidated[30]. One known mechanism describes that verteporfin blocks the YAP-TEAD regulation complex formation, which locates within the cell nucleus[27,31]. Others reported that in the presence of p53, verteporfin increases the expression of the

chaperon protein 14-3-3σ, which in turn promotes cytoplasmic localization of YAP (i.e. inhibits nuclear translocation of YAP)[32]. Conversely, when p53 was knocked down, the ability of verteporfin to enhance 14-3-3α was attenuated[32]. This implies that if higher p53 expression levels exist in a cell, it is likely to respond more significantly to verteporfin treatment and demonstrate more pronounced changes in the extent of cytoplasmic localization of YAP (i.e. decreased nuclear localization of YAP). Our results show that upon verteporfin treatment, indeed, less nuclear localization of YAP was seen in Day 3 newly form OL than Day 10 myelinating OLs (Supplementary Figure 7). This observation is consistent with the proposed mode of action by verteporfin because newly formed OLs do indeed express higher levels of p53 than myelinating OLs[33].

Altogether, these observations highlight the verteporfin effect and the possible involvement of alternative pathways that rescue the YAP nuclear import. Since the exact working mechanisms of verteporfin on OPCs and OLs have not been studied in detail, future studies could focus on this aspect. It is also noteworthy that YAP keeps shuttling between cytoplasm and nucleus, irrespectively of cell tension[34] and that YAP relocalization is rapid (30 min) and reversible[19], which makes the interpretation of the long-term study of YAP localization dicey when using verteporfin. Nevertheless, we deducted from our results that YAP mechanotransduction pathway is involved in OL myelination and to a lesser extent, in OPC differentiation.

The versatility of our artificial axon platform allows one to analyze the effects of axon intrinsic and axon structural stiffness on the fate of OLs. Our system is derived from the electrospinning technique that was used to obtain artificial axons that are capable of

supporting oligodendrocyte myelination[9,13,14,35,36]. However, we have upgraded several features (suspended fibers, controlled fiber diameter, length, and density), especially the tunable stiffness characteristic. Hence, we ensured preserved fiber properties over the different stiffness, thereby guaranteeing seeded cells the same chances of encountering fibers. This system is flexible and easily adaptable to diverse materials hence allowing one to change the intrinsic stiffness of the fibers by orders of magnitude (2-3,000 MPa) through the appropriate selection of polymers (gelatin, PLA and PCL). We used conventional materials that are readily available commercially and frequently utilised in tissue engineering[9,14,37]. We believe that in order to further decrease fiber intrinsic stiffness down to the Pa/kPa range, novel materials derived by materials engineering would be necessary.

Our platform is primarily inspired by the micropillars systems, leading us to incorporate structural mechanics considerations during the design process. Thus, similar to traction force microscopy[6,7], we also designed the platform to be optically visible, allowing fluorescent imaging. Furthermore, we have engineered the fiber platform to be compatible with laser microdissection (LMD) (Supplementary Figure 8) to allow the identification and extraction of cells or parts of a cell[38,39] (e.g. myelin sheaths of interest). These isolated cells/ cellular components may then be pooled and analyzed to characterize cell phenotypic changes and possible mechanotransduction pathways. Given the optical visibility, we envision this platform to be suitable for live cell imaging as well.

We and others have shown that OLs form myelin sheaths of physiological length on electrospun fibers whose diameters match that of CNS axons (0.5-2 µm)[9,14]. With this configuration, we were able to obtain more morphologically complete myelin sheaths for analysis as compared to other studies[13,40]. Our results also suggest that mechanical stiffness

distinctively influences OL differentiation and myelination. Although diseased brain is often physically stiffer as compared to normal brain[4,41], studies focused on MS using different methodologies still argue controversial results[24]. Specifically, the increase in fibrillar collagen results in perivascular fibrosis[3]. This disturbs the control of ECM secretion by glial cells and leads to an increase in proteoglycan secretion that accumulates at the proximity of demyelinated axons and contributes to local increase in tissue stiffness [42,43]. However, the tissue mechanical properties in demyelinating diseases depend on the severity and chronicity of the pathology. Chronic demyelination, as in the case of multiple sclerosis, led to an increase in tissue rigidity[24, 44]. Hence, our results showing impaired myelination in stiffer condition may be consistent. From another perspective, our data could also suggest that a controlled, sequential switch from a stiff (to promote OPC differentiation) to a compliant (to enhance OL myelination) substrate may be useful for achieving remyelination.

Notwithstanding, literature reported different effects of the substrate stiffness-directed OL differentiation, which could be linked to the nature of the coating on the substrate, in particular laminin 2[11,4]. Laminin 2 itself results in the activation of intracellular signals through the pathways regulated by integrins interacting with the ECM and actomyosin network[45], while PDL is not known to mobilize integrins nor activate intracellular signaling. Possible future work could focus on comparing the effect of the coating (e.g. ECM proteins vs. PDL) applied to the same artificial axons on the differentiation of OLs.

Given our observations that stiffness promotes OPC differentiation but impedes OL myelination, we emphasize that the research of therapeutics focusing on enhancing CNS myelination must realize that differentiation and myelination may be independently

regulated. Therefore, current drugs that aim at promoting differentiation, assuming this will lead to myelination, needs to be reconsidered. Our platform is, thus, expected to contribute effectively to drug discovery programmes in testing molecules that could improve OL differentiation as well as myelination. Another consideration could also be the timely administration of drugs that are related to mechanosensing, as a way to enhance OL differentiation or myelination, depending on the conditions of the microenvironmental stiffness.

The stiffness of a fully developed rat brain measured here is consistent with other studies in magnitude[3,46], which ranges between 100 to 400 Pa on average. Although we admit a vast stiffness difference between our *in vitro* platform (from 0.014 N/m to 0.050 N/m) and the developing rat brain (50-100 times weaker), we still managed to observe the myelination of artificial axons. Besides, one should keep in mind that the brain tissue is highly heterogeneous with a varied and dynamic matrix component which is responsible for the very local alteration of structural stiffness, making comparisons with matrices consisting of a single polymer relatively complex. These reasons, therefore, prompt us to consider that in the physiological context, stiffness is most likely to be one of the many factors regulating myelination. Notwithstanding, micropillars studies (from which our system was inspired) have measured a substrate stiffness ranging from 0.47x10-3 to 0.174 N/m[6,7] with an intrinsic stiffness ranging from 1.5 to 2.5 MPa[7], which is also within the stiffness range of our platform. To date, there is no system available, which better mimics the physiology of the CNS by reproducing both topography and structural stiffness to study the behavior of glial cells in response to stiffness changes. Hence, there may also exist factors that heighten or amplify the mechanosensing abilities of OPCs/OLs *in vivo*, which are lacking in the *in vitro*

environment, such that they are able to differentiate structural stiffness values within a few hundreds of Pascals. Particularly, OL myelination and remyelination is a very complex process and depends on both biochemical and biophysical inputs[41,47]. Additionally, biochemical signalling may at times be so inhibitory that it greatly overcomes the biophysical aspect of this regulation, as observed in traumatic injuries. It is noteworthy that biochemical signalling greatly varies during development and in disease context. We demonstrated that electrospun fibers are suitable for incorporating drugs and genes[14,35,48] for screening purposes with good correlation between *in vitro* and *in vivo* regenerative outcomes[48]. Future studies could then include the synergistic combination of biochemicals (e.g. promyelinogenic factors like miR-219/miR-338[49-52] with mechanical stiffness changes to verify the synergistic, antagonistic or possible recovery effects.

Another drawback is the current methodology that has been used to measure the stiffness of neuronal axons. Specifically, in those studies, neurons are generally grown on 2D substrates, such as glass[17, 53]. The great stiffness of glass can lead to changes in cytoskeletal polymerization and structure, which in turn alter cell rigidity[53,54]. Consequently, this remains a major constraint in order to be able to strictly define the natural axonal stiffness encountered in the CNS, making the comparison with the intrinsic stiffness of biomimicking materials difficult. Herein, we manipulated commonly used materials as proof-of-principle to establish the tunable stiffness features of the platform, although these materials demonstrated high intrinsic stiffness in the MPa range, which could be greater than physiological axon stiffness. We would, therefore, require a more thorough profiling of the actual axon stiffness to be able to further optimize our artificial axon platform. From the engineering perspective, our system can be further improved by designing novel softer

electrospinnable and structurally stable materials, which could yield the ideal physiological intrinsic stiffness. Even though there is currently a mechanical mismatch, the important and interesting thing is that we can still see oligodendroglial cells reacting to the range of stiffnesses imposed by our platform. Generally, the range of substrate stiffness to which different cells response differs with cell types. Fibroblasts, for instance, respond differently in terms of cell morphology and motility towards substrates of stiffness ranging from about 14 kPa to 30 kPa[55] (which in the case of neurons, appears to be substrates of infinite hardness, like a glass substrate), while these cells appeared to have little changes in response towards stiffness in the range of 50-500 Pa, which is the range of stiffness that showed profound changes in neurite extension in neurons[56].

Extending from the observations derived from our study, it may be possible to manipulate mechanotransducers so as to 'trick' the oligodendroglial lineage cells into thinking that the stiffness of their surroundings has changed. As identified by us using artificial axons and Shimizu, *et al.*, using 2D substrates[20], the YAP/TAZ pathway could be a potential target. Similarly, Segel, *et al.* showed that Piezo1[4] (a key mediator in mechanical signalling) may be an alternative. Altogether, the novel assay that we describe here may help further our understanding on mechanotransduction response of OL myelination. Based on our successful proof of principle, this platform may, therefore, be used in future studies to elucidate other mechanotransduction pathways that have been reported to play prominent roles in OL differentiation (e.g. piezo1[4], myosin II[57], or the laminin2-integrin interaction[58]), and it can also be used to elucidate new pathways specific to OL myelination. It may also have considerable utility as part of a drug discovery programme in determining whether this is the case and identifying those that promote both differentiation and myelination.

Conclusion

In this study, we report a novel suspended fiber platform for systematic understanding of cell mechanotransduction. Specifically, we utilized classical structural mechanics principles to derive a platform that allows the independent variation of fiber intrinsic stiffness and structural stiffness by simply changing polymer crystallinity, crosslinking extent, fiber suspension length or fiber diameter. With this versatile and unique system, we provide two important conclusions. First, the increased ECM stiffness in chronic MS lesions would be predicted to limit remyelination, despite any increase in OL number. Second, the opposing effects on differentiation and myelination emphasize that these two phases of OL maturation are regulated independently, a conclusion that has important implications for current work screening for small molecules or drugs that enhance differentiation as an approach to regenerative therapies in MS. The benefits of such drugs may be limited by stiffness-associated effects on myelination. The novel assay we describe here may help further our understanding on mechanotransduction response of OL myelination. It may also be used for drug discovery to identify candidates that promote both differentiation and myelination. Since fiber topography closely mimics the extracellular matrix architecture, these constructs may also be applicable to other mechanotransduction analyses involving other cell types.

Acknowledgements

This work was supported partially by the Singapore National Research Foundation under its NMRC-CBRG grant (NMRC/CBRG/0096/2015), administered by the Singapore Ministry of Health's National Medical Research Council, and also by the MOE Tier 1 grant (RG38/19). The

NTU Research Scholarship supporting W. Ong and J. Lin is also acknowledged.

Contributions

S. Y. Chew conceived and was in charge of overall planning and direction of the experiments. W. Ong, N. Marinval, J. Lin, M. H. Nai, Y. S. Chong and C. Pinese performed experiments. W. Ong fabricated and characterized scaffolds, isolated and seeded primary rat OPCs, performed immunostaining followed by imaging and quantification of samples for Figure 1, 2 and 3 and Supplementary Figure 1, 2, 3, 4 and 5. N. Marinval fabricated and characterized scaffolds, isolated and seeded primary rat OPCs, performed immunostaining followed by imaging and quantification of samples for Figure 4 and Supplementary Figure 2, 7 and 8. J. Lin, M. H. Nai and Y. S. Chong contributed to Figure 6. M. H. Nai contributed to all AFM experiments. Y. S. Chong performed all brain slices sectioning. C. Pinese fabricated and characterized PLA polymers and provided Supplementary Figure 6. M. E. Bechler and C. ffrench-Constant contributed to experimental logic, result interpretation and manuscript preparation. W. Ong, N. Marinval, J. Lin, S. Sajikumar, C. T. Lim, M. E. Bechler and S. Y. Chew edited and proofread the manuscript. S. Y. Chew guided the project and provided the funding.

Competing interests

The authors declare no competing interests.

References

[1] A. J. Engler, S. Sen, H. L. Sweeney, D. E. Discher, *Cell*. **2006**, *126*, 677-689.

[2] T. Mammoto, D. E. Ingber, *Development*. **2010**, *137*, 1407-1420.

[3] E. Moeendarbary, I. P. Weber, G. K. Sheridan, D. E. Koser, S. Soleman, B. Haenzi, E. J. Bradbury, J. Fawcett, K. Franze, *Nat. Commun*. **2017**, *8*, 1–11.

[4]. M. Segel, B. Neumann, M. F. E. Hill, I. P. Weber, C. Viscomi, C. Zhao, A. Young, C. C. Agley, A. J. Thompson, G. A. Gonzalez, A. Sharma, S. Holmqvist, D. H. Rowitch, K. Franze, R. J. M. Franklin, K. J. Chalut, *Nature*. **2019**, *573*, 130–134.

[5] T. Lourenço, J. Paes de Faria, C. A. Bippes, J. Maia, J. A. Lopes-da-Silva, J. B. Relvas, M. Grãos, *Sci. Rep*. **2016**, *6*, 21563.

[6] C. G. Galbraith, M. P. Sheetz, *Proc. Natl. Acad. Sci. U. S. A*. **1997**, *94*, 9114–9118.

[7] O. du Roure, A. Saez, A. Buguin, R. H. Austin, P. Chavrier, P. Silberzan, B. Ladoux, *Proc. Natl. Acad. Sci. U. S. A.* **2005**, *102*, 2390 LP – 2395.

[8] S. S. Rosenberg, E. E. Kelland, E. Tokar, A. R. De La Torre, J. R. Chan, *Proc. Natl. Acad. Sci.* **2008**, *105*, 14662–14667.

[9] M. E. Bechler, L. Byrne, C. Ffrench-Constant, *Curr. Biol*. **2015**, *25*, 2411–2416.

[10] A. Jagielska, A. L. Norman, G. Whyte, K. J. Van Vliet, J. Guck, R. J. M. Franklin, *Stem Cells Dev*. **2012**, *21*, 2905–2914.

[11] M. M. Urbanski, L. Kingsbury, D. Moussouros, I. Kassim, S. Mehjabeen, N. Paknejad, C. V. Melendez-Vasquez, *Sci. Rep*. **2016**, *6*, 1–12.

[12] H. Cao, T. Liu, S. Y. Chew, *Adv. Drug Deliv. Rev*. **2009**, *61*, 1055–1064.

[13] S. Lee, S. Y. C. Chong, S. J. Tuck, J. M. Corey, J. R. Chan, *Nat Protoc*. **2013**, *8*, 771-782.

[14] W. Ong, J. Lin, M. E. Bechler, K. Wang, M. Wang, C. Ffrench-Constant, S. Y. Chew, *Acta Biomater*. **2018**, *75*, 152–160.

[15] P. L. Lamoureux, M. R. O'Toole, S. R. Heidemann, K. E. Miller, *BMC Neurosci*. **2010**, *11*, 140.

[16] C. Fressinaud, R. Berges, J. Eyer, *Neurochem Int*. **2012**, *60*, 78-90.

[17] E. Spedden, J. D. White, E. N. Naumova, D. L. Kaplan, C. Staii, *Biophys J*. **2012**, *103*, 868-877.

[18] R. de Rooij, E. Kuhl, *Biophys J*. **2018**, *114*, 201-212.

[19] S. Dupont, L. Morsut, M. Aragona, E. Enzo, S. Giulitti, M. Cordenonsi, F. Zanconato, J. Le Digabel, M. Forcato, S. Bicciato, N. Elvassore, S. Piccolo, *Nature*. **2011**, *474*, 179–83.

[20] T. Shimizu, Y. Osanai, K. F. Tanaka, M. Abe, R. Natsume, K. Sakimura, K. Ikenaka, *Glia*. **2017**, *65*, 360–374.

[21] A. Jagielska, A.L. Lowe, E. Makhija, L. Wroblewska, J. Guck, R.J.M. Franklin, G. V. Shivashankar, K.J. Van Vliet, *Front. Cell. Neurosci*. **2017**, 11, 1–16.

[22] N. Downes, P. Mullins, *Toxicologic Pathology*. **2013**, *42*, 913-922.

[23] R. J. M. Franklin, C. Ffrench-Constant, *Nat. Rev. Neurosci*. **2017**, *18*, 753-769.

[24] M.M. Urbanski, M.B. Brendel, C. V. Melendez-Vasquez, *Sci. Rep*. **2019**, *9*, 1–13.

[25] Y. Poitelon, C. Lopez-Anido, K. Catignas, C. Berti, M. Palmisano, C. Williamson, D. Ameroso, K. Abiko, Y. Hwang, A. Gregorieff, J.L. Wrana, M. Asmani, R. Zhao, F.J. Sim, L. Wrabetz, J. Svaren, M.L. Feltri, *Nat. Neurosci.* **2016**, *19*, 879–887.

[26] M. Grove, H. Kim, M. Santerre, A.J. Krupka, S.B. Han, J. Zhai, J.Y. Cho, R. Park, M. Harris, S. Kim, B.E. Sawaya, S.H. Kang, M.F. Barbe, S.H. Cho, M.A. Lemay, Y.J. Son, *Elife*. **2017**, *6*, 1–27.

[27] Y. Liu-Chittenden, B. Huang, J.S. Shim, Q. Chen, S.-J. Lee, R.A. Anders, J.O. Liu, D. Pan, *Genes Dev*. **2012**, *26*, 1300–1305.

[28] S. Mascharak, P.L. Benitez, A.C. Proctor, C.M. Madl, K.H. Hu, R.E. Dewi, M.J. Butte, S.C. Heilshorn, *Biomaterials*. **2017**, *115*, 155–166.

[29] G. Chu, Z. Yuan, C. Zhu, P. Zhou, H. Wang, W. Zhang, Y. Cai, X. Zhu, H. Yang, B. Li, *Acta Biomater*. **2019**, *92*, 254–264.

[30] P.C. Calses, J.J. Crawford, J.R. Lill, A. Dey, *Trends in Cancer*. **2019**, *5*, 297–307.

[31] G.M. Elisi, M. Santucci, D. D'arca, A. Lauriola, G. Marverti, L. Losi, L. Scalvini, M.L. Bolognesi, M. Mor, M.P. Costi, *Cancers (Basel)*. **2018**, *10*.

[32] C. Wang, X. Zhu, W. Feng, Y. Yu, K. Jeong, W. Guo, Y. Lu, G.B. Mills, *Am. J. Cancer Res*. **2016**, *6*, 27–37.

[33] Y. Zhang, K. Chen, S.A. Sloan, M.L. Bennett, A.R. Scholze, S. O'Keeffe, H.P. Phatnani, P. Guarnieri, C. Caneda, N. Ruderisch, S. Deng, S.A. Liddelow, C. Zhang, R. Daneman, T. Maniatis, B.A. Barres, J.Q. Wu, *J. Neurosci*. **2014**, *34*, 11929–11947.

[34] A. Das, R.S. Fischer, D. Pan, C.M. Waterman, J. Biol. Chem. **2016**, *291*, 6096–6110.

[35] H. J. Diao, W. C. Low, U. Milbreta, Q. R. Lu, S. Y. Chew, *Journal of controlled release : official journal of the Controlled Release Society*. **2015**, *208*, 85-92.

[36] H.J. Diao, W.C. Low, Q.R. Lu, S.Y. Chew, *Biomaterials*. **2015**, *70*, 105–114.

[37] S. Baiguera, C. Del Gaudio, E. Lucatelli, E. Kuevda, M. Boieri, B. Mazzanti, A. Bianco, P. Macchiarini, *Biomaterials*. **2014**, *35*, 1205–1214.

[38] P. Civita, S. Franceschi, P. Aretini, V. Ortenzi, M. Menicagli, F. Lessi, F. Pasqualetti, A. Giuseppe Naccarato, C. Maria Mazzanti, *Front. Oncol*. **2019**, *9*, 1–12.

[39] Z. Zeng, N. Miao, T. Sun, *Stem Cell Res. Ther*. **2018**, *9*, 1–11.

[40] D. Espinosa-Hoyos, A. Jagielska, K. A. Homan, H. Du, T. Busbee, D.G. Anderson, N. X. Fang, J. A. Lewis, K. J. Van Vliet, *Sci. Rep*. **2018**, *8*, 1–13.

[41] N. G. Bauer, C. Ffrench-Constant, *J. Biol*. **2009**, *8*.

[42] S.A. Back, T.M.F. Tuohy, H. Chen, N. Wallingford, A. Craig, J. Struve, L.L. Ning, F. Banine, Y. Liu, A. Chang, B.D. Trapp, B.F. Bebo, M.S. Rao, L.S. Sherman, *Nat. Med*. **2005**, *11*, 966–972.

[43] G. Yiu, Z. He, *Nat. Rev. Neurosci*. **2006**, *7*, 617–627.

[44] H. Mohan, M. Krumbholz, R. Sharma, S. Eisele, A. Junker, M. Sixt, J. Newcombe, H. Wekerle, R. Hohlfeld, H. Lassmann, E. Meinl, *Brain Pathol*. **2010**, *20*, 966–975.

[45] A. Kippert, D. Fitzner, J. Helenius, M. Simons, *BMC Cell Biol*. **2009**, *10*, 71.

[46] K. Holtzmann, H. O. B. Gautier, A. F. Christ, J. Guck, R. T. Káradóttir, K. Franze, J. *Neurosci. Methods*. *2016*, *271*, 50–54.

[47] H. S. Domingues, C. C. Portugal, R. Socodato, J. B. Relvas, *Front. Cell Dev. Biol*. **2016**, *4*, 1–16.

[48] N. Zhang, U. Milbreta, J. S. Chin, C. Pinese, J. Lin, H. Shirahama, W. Jiang, H. Liu, R. Mi, A. Hoke, W. Wu, S. Y. Chew, *Adv Sci*. **2019**, *6*.

[49] J. C. Dugas, T. L. Cuellar, A. Scholze, B. Ason, A. Ibrahim, B. Emery, J. L. Zamanian, L. C. Foo, M. T. McManus, B. A. Barres, *Neuron*. **2010**, *65*, 597–611.

[50] X. Zhao, X. He, X. Han, Y. Yu, F. Ye, Y. Chen, T. Hoang, X. Xu, Q.-S. Mi, M. Xin, F. Wang, B. Appel, Q.R. Lu, *Neuron*. **2010**, *65*, 612–626.

[51] H. Wang, A. L. Moyano, Z. Ma, Y. Deng, Y. Lin, C. Zhao, L. Zhang, M. Jiang, X. He, Z. Ma, F. Lu, M. Xin, W. Zhou, S. O. Yoon, E. R. Bongarzone, Q. R. Lu, *Dev. Cell*. **2017**, *40*, 566-582.e5.

[52] U. Milbreta, J. Lin, C. Pinese, W. Ong, J. S. Chin, H. Shirahama, R. Mi, A. Williams, M.E. Bechler, J. Wang, C. ffrench-Constant, A. Hoke, S. Y. Chew, *Mol. Ther*. **2019**, *27*, 411–423.

[53] Y.B. Lu, K. Franze, G. Seifert, C. Steinhäuser, F. Kirchhoff, H. Wolburg, J. Guck, P. Janmey, E.Q. Wei, J. Käs, A. Reichenbach, *Proc. Natl. Acad. Sci. U. S. A*. **2006**, *103*, 17759–17764.

[54] K. Franze, P.A. Janmey, J. Guck, *Annu. Rev. Biomed. Eng*. **2013**, *15*, 227–251.

[55] C.M. Lo, H.B. Wang, M. Dembo, Y.L. Wang, Biophys. J. 2000, 79, 144–152.

[56] L.A. Flanagan, Y. El Ju, B. Marg, M. Osterfield, P.A. Janmey, Neuroreport. 2002, 13, 2411–2415.

[57] H. Wang, A. Tewari, S. Einheber, J.L. Salzer, C. V. Melendez-Vasquez, J. Cell Biol. 2008, 182, 1171–1184.

[58] P.C. Buttery, C. Ffrench-Constant, Mol. Cell. Neurosci. 1999, 14, 199–212.

[59] G. Schwach, J. Coudane, R. Engel, M. Vert, Polymer International. 1998, 46, 177-182.

[60] C. Pinese, A. Leroy, B. Nottelet, C. Gagnieu, J. Coudane, X. Garric, J. Biomed. Mater. Res. - Part B Appl. Biomater. 2017, 105, 735–743.

Methods

Materials

Polycaprolactone (PCL, Mw: 200,000) was purchased from PolySciTech, Polycaprolactone (PCL, Mw: 45,000), 2,2,2-trifluoroethanol (TFE), DNase 1 type IV, Poly-D-Lysine (PDL), N-Acetyl-L-Cysteine (NAC), D-biotin, ITS, Putrescine, L-Thyroxine (T4), Tri-iodothyroxine (T3), Progesterone, Bovine Serum Albumin (BSA), L-cysteine, Triton X-100 were purchased from Sigma-Aldrich. Alexa-Fluor 488 goat anti-rat, Alexa-Fluor 633 goat anti-rabbit antibodies, minimum essential media (MEM), DMEM High Glucose, Penicillin/Streptomycin (Pen/Strep) were purchased from Life Technologies. NS21 supplement and Neuro Medium were purchased from Miltenyi Biotech. Rat anti-Myelin Basic Protein (MBP, aa82-87) was purchased from Bio-Rad. Rabbit anti-Oligodendrocyte Transcription Factor 2 (Olig2, AB9610) was purchased from Merck. Rabbit anti-YAP (D8H1X) was purchased from Cell Signalling Technology. Papain suspension was purchased from Worthington.

Preparation of Coronal Brain Slices for AFM Indentations

Female Sprague Dawley rats (P5, P15 and P35) were used to prepare coronal brain slices for AFM indentation experiments. The rats were euthanized with ice (P5 rats) and CO_2 (P15 and P35 rats) before decapitation. The whole brain was then gently removed and kept in cooled (4°C) artificial cerebrospinal fluid (aCSF) saturated with carbogen (95% O_2, 5% CO_2; flow rate = 16 L/h). The composition of aCSF is as follows: 124.0 mM NaCl, 3.7 mM KCl, 1.0 mM $MgSO_4 \bullet 7H_2O$, 2.5 mM $CaCl_2$, 1.2 mM KH_2PO_4, 24.6 mM $NaHCO_3$, and 10 mM D-glucose. Coronal brain slices were then cut at 400 µm thickness using a vibratome (VT 1200S, Leica Biosystems) and immediately transferred into a 60 mm diameter petri dish filled with cooled, carbogenated aCSF to preserve their integrity. To ensure that the brain slices remained

mechanically intact, all samples were tested under the atomic force microscope (AFM) within 3 h. Additionally, these brain slices were mounted onto a glass slide using cyanoacrylate-based glue before AFM mechanical indentations.

Fabrication of Tunable Stiffness Platform

Supplementary Figure 2 illustrates the engineering of the tunable stiffness microfiber platform. PCL pellets (MW: 45,000) were pressed into 50 µm PCL film with a heat press and cut into a thin frame with a customized cutter (Outer area: 11.5 cm x 1.5 cm, Inner area: 9.5 cm x 1 cm). The thin PCL film was mounted onto an electrically conductive wheel for electrospinning to collect electrospun PCL fibers.

PCL pellets were also pressed into 0.5 mm thick film and cut into frames of different dimensions with customized cutters. PCL frames were used to secure fibers from the same sheet of thin film with silicone glue. Inverting the scaffold creates a 0.5 mm suspended fiber structure for OPCs seeding.

Scanning Electron Microscopy

The morphology of the microfibers was evaluated using scanning electron microscopy (SEM) (JEOL, JSM-6390LA, Japan). Briefly, PCL substrates were attached onto the SEM support by carbon tapes and sputter-coated with platinum for 60 s at 20 mA. Thereafter, the samples were imaged using an accelerating voltage of 10 kV.

Atomic Force Microscopy (AFM)

The substrate bending experiments were performed using a Dimension Icon AFM (Bruker). Force curves were obtained using the peakforce quantitative nanomechanical (QNM) fluid mode of the AFM. The probe consisted of a 25 μm diameter polystyrene bead attached to a silicon nitride cantilever with a spring constant of 0.406 N/m (Novascan Technologies, Inc., Ames, IA). The suspended microfiber scaffold was fixed on both ends and immersed in PBS with 0.1% BSA added. A maximum force of 10 nN and loading rate of 8 μm/s were applied to ensure the microfiber scaffold undergoes elastic bending. At least 8 force curves across the midspan of each suspended microfiber scaffold were obtained. The slope of the force-distance curve which corresponds to the stiffness (N/m) was extracted using the Nanoscope analysis software v1.9.

Single fiber indentations were performed at room temperature in liquid media (PBS with 0.1% BSA) using a Dimension Icon AFM (Bruker) in peakforce quantitative nanomechanical mapping mode. A rectangular AFM probe with a nominal spring constant of 200 N/m and tip radius of 8 nm (Tap525, Bruker) was used to test the mechanical properties of PCL and PLA fibers. Gelatin fibers were tested using a triangular AFM probe with a nominal spring constant of 0.7 N/m and tip radius of 20 nm (ScanAsyst-Fluid, Bruker). Electrospun fibers resting on glass were indented and the force-displacement data were fitted to the DMT model to extract the modulus using Nanoscope analysis software v1.9.

Force measurements were carried out at room temperature in liquid media (aCSF) using a Nanowizard 4 BioScience AFM (JPK Instruments, Germany). Indentations were performed at the cortex and corpus callosum of the brain slices. The AFM probe consisted of a 4.5 μm diameter polystyrene bead attached to a silicon nitride cantilever (Novascan

Technologies Inc., Ames, IA). The nominal spring constants of the cantilever used was 0.03 N/m. A maximum force of 1 nN and loading rate of 10 μm/s were applied. The modulus values were calculated for each recorded curve using JPK Data Processing Software (JPK Instruments, Germany), which employs a Hertz's contact model for spherical indenters (diameter of 4.5 μm; Poisson's ratio of 0.5) fitted to the extend curves.

Synthesis of Poly(Lactic Acid)

We varied the percentage of L-lactic acid contained in the poly(lactic acid) in order to vary the intrinsic stiffness without changing the surface chemical properties of the polymer. PLA94 and PLA50 (containing 94% and 50% L-lactic acid and 6% and 50% L-lactic acid, respectively) of 200,000 g/mol were synthesized through ring opening polymerization as reported previously[59,60]. Briefly, predetermined amounts of dry D,L-lactide, L,L-lactide, benzyl alcohol and tin(II) 2-ethylhexanoate (0.1 molar % with respect to lactic acid units) were introduced into a dry flask. After five argon/vacuum alternations to remove oxygen, the flasks were sealed and placed 5 days under rotation at 130°C to allow polymerization. Then, the polymers were solubilized in dichloromethane and precipitated in cold diethyl ether. Finally, the product was dried under reduced pressure.

^{1}H NMR spectra were recorded at room temperature using an AMX300 Bruker spectrometer at 300 MHz. Chemical shifts were referenced to the peak of deuterated chloroform (Supplementary Figure 6).

X-ray Diffraction and Differential Scanning Calorimetry

PLA degree of crystallinity analysis was performed with x-ray diffraction (XRD) Bruker D2 Phaser according to manufacturer protocol. PLA samples were loaded onto a clean sample holder and scanned with a range of 5.0 to 80.0 degree at 0.02 degree step width. Background was removed with Bruker analysis software and raw data was exported into excel spreadsheet. Absolute intensity at every point was then plotted in Graphpad Prism to visualize the location of peaks and relative peak intensity of PLA_{50} and PLA_{94}.

Differential scanning calorimetry (DSC) measurements were carried out under nitrogen on a Perkin Elmer Instrument DSC 6000 Thermal Analyzer. Samples were subjected to a thermal analysis first by heating to 300°C (10 °C/min), followed by cooling (10 °C/min from 300 °C to 0 °C) and then a second heating to 300°C (10 °C/min). Glass transition temperature (T_g), melting temperature (T_m), calorific capacity (ΔC_p) and melting enthalpy (ΔH_m) were measured on the first heating ramp (Supplementary Figure 6).

OPCs Isolation and Myelination Culture

The isolation of primary OPCs from rats was approved by the Institutional Animal Care and Use Committee (IACUC, Protocol number: A0333) at Nanyang Technological University, Singapore. The isolation and culture of primary OPCs and the myelination culture were described in our previous work[14]. Briefly, P0-P2 neonatal rat cortices that were cleaned from meninges were enzymatically digested with 1.2 U Papain and 40 µg/ml DNase at 37 ^{o}C for 1 h. Thereafter, the enzymatic activity was stopped with 8 ml of DMEM with 10% Fetal Bovine Serum (FBS) and the dissociated tissues were triturated with a 21G needle and syringe. Tissues from 6 digested cortices were seeded onto 4 PDL-coated T75 flasks and cultured in DMEM with 10% FBS and 1% Pen/Strep. After 9-11 days, the OPCs were separated from the

mixed glia culture by shaking on an orbital shaker at 200 rpm for 1 h at 37 °C to remove the loosely attached microglia. This was followed by a further 16-17 h of shaking. OPCs were then further purified by differential adhesion on untreated petri dishes for 25 min. Purified OPCs were then homogeneously and evenly seeded at a density of 10,000/cm2, which was optimized for culture onto each suspended fiber substrate[14], and cultured in myelin medium , which consisted of DMEM:Neurobasal (50:50), NS21, 1% Pen/Strep, Glutamax, ITS, 10 ng/ml biotin, 5 µg/ml NAC and SATO (100 µg/ml BSA, 60 ng/ml Progesterone, 16 µg/ml Putrescine, 400 ng/ml T3 and T4).

Immunofluorescent Staining

After 3 or 10 days of culture on the suspended fibers, the cells were fixed with 4% paraformaldehyde (PFA). The fixed myelin-fiber cultures were then permeabilized with 0.1% Triton-X for 15 min at room temperature. Next, the samples were incubated with primary antibodies overnight at 4 °C, followed by secondary antibodies for 1 h at room temperature. The primary antibodies used were: rat anti-MBP (1:200) and rabbit anti-Olig2 (1:1000). The secondary antibodies used were: Alexa-Fluor 488 goat anti-rat and Alexa Fluor 633 goat anti-rabbit (both at 1:1000). The nuclei were counterstained with DAPI. The samples were then mounted onto 60 mm coverglass with Fluoromount-G and imaged under a Zeiss LSM 800 confocal microscope. OPC differentiation and myelination were quantified as described in our previous work[14]. Briefly, only cells that attached to the fibers were counted, whereas cells that have fallen through the scaffold were ignored. Single cells were evenly distributed along the fibers and cell imaging was performed in a random fashion along the midline or the edge lines For each scaffold, 10-15 images were performed to obtain a sufficient number of cells (≥ 30) to address OL differentiation and myelination. To measure the implication of YAP

mechanotransduction pathway, the specific inhibitor of YAP transcription activity, verteporfin (0.1 μM), or DMSO (vehicle control) were added in the myelin medium 5 days after cell seeding onto scaffolds and sustained in the culture medium until cell fixation to affect specifically the myelination process.

Statistical Analysis

All values were presented as mean ± standard deviation (S.D). Student's t-test was used to compare between 2 independent samples. Levene's test of homogeneity was used to check for homogeneity of variance when comparing 3 or more sample groups. One-way ANOVA with Tukey post-hoc test was used for samples that passed the homogeneity test. Otherwise, non-parametric Kruskal-Wallis pair-wise comparison was made. P-values of less than 0.05 were considered to be statistically significant.

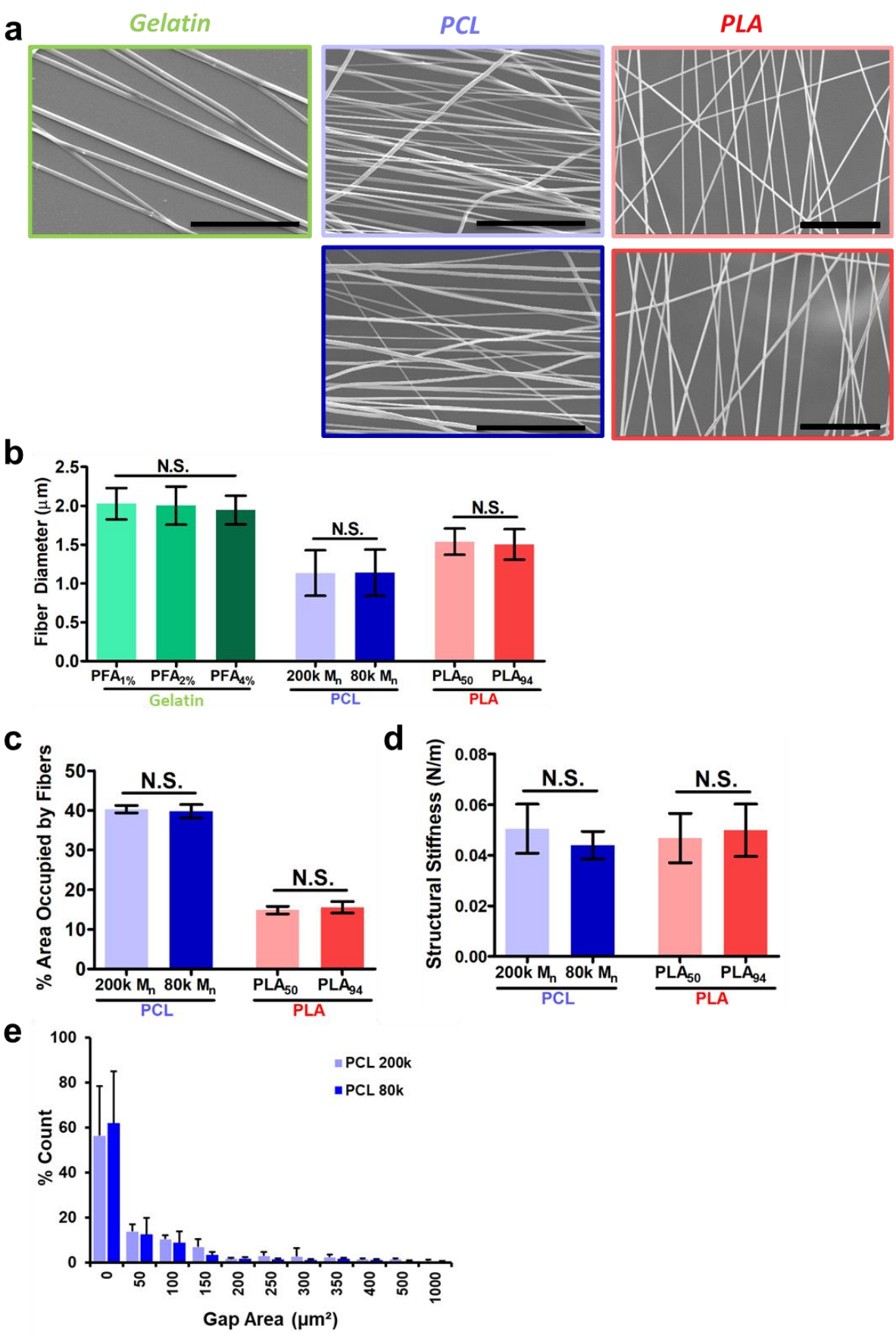
a
Gelatin
PCL
PLA
b
Fiber Diameter (μm)
2.5
2.0
1.5
1.0
0.5
0.0
N.S.
N.S.
N.S.
PFA1%
PFA2%
PFA4%
200k Mn
80k Mn
PLA50
PLA94
Gelatin
PCL
PLA
c
% Area Occupied by Fibers
50
40
30
20
10
0
N.S.
N.S.
200k Mn
80k Mn
PLA50
PLA94
PCL
PLA
d
Structural Stiffness (N/m)
0.08
0.06
0.04
0.02
0.00
N.S.
N.S.
200k Mn
80k Mn
PLA50
PLA94
PCL
PLA
e
% Count
100
80
60
40
20
0
PCL 200k
PCL 80k
0
50
100
150
200
250
300
350
400
500
1000
Gap Area (μm²)

Supplementary Figure 1. Same material could be engineered to possess similar physical properties even though intrinsic stiffness was varied. (a) Scanning electron microscopy images show similar polymeric fiber formed from electrospinning with gelatin, PCL and PLA. Scale bar represents 50 µm. **(b)** Data shows artificial axons from all polymer has similar fiber diameter within each polymer class. N.S. non-statistical significance. One-way ANOVA with Tukey post-hoc for gelatin samples, independent t-test for PCL and PLA samples. **(c)** Data shows artificial axons from PCL and PLA has similar fiber density, regardless of intrinsic stiffness and diameter. N.S. non-statistical significance. Independent t-test for PCL and PLA samples. **(d)** Data shows artificial axons from PCL and PLA has similar structural stiffness, regardless of intrinsic stiffness and diameter. N.S. non-statistical significance. Independent t-test for PCL and PLA samples. **(e)** Data show the distribution of the scaffold gap area. The gap measurements were performed on SEM images obtained from scaffolds (PCL 80k and 200k) at low magnification (x500). The gap distribution shows a high proportion of small gaps (< 50 μm^2) while large gaps (≥ 200 μm^2) remain as the minority.

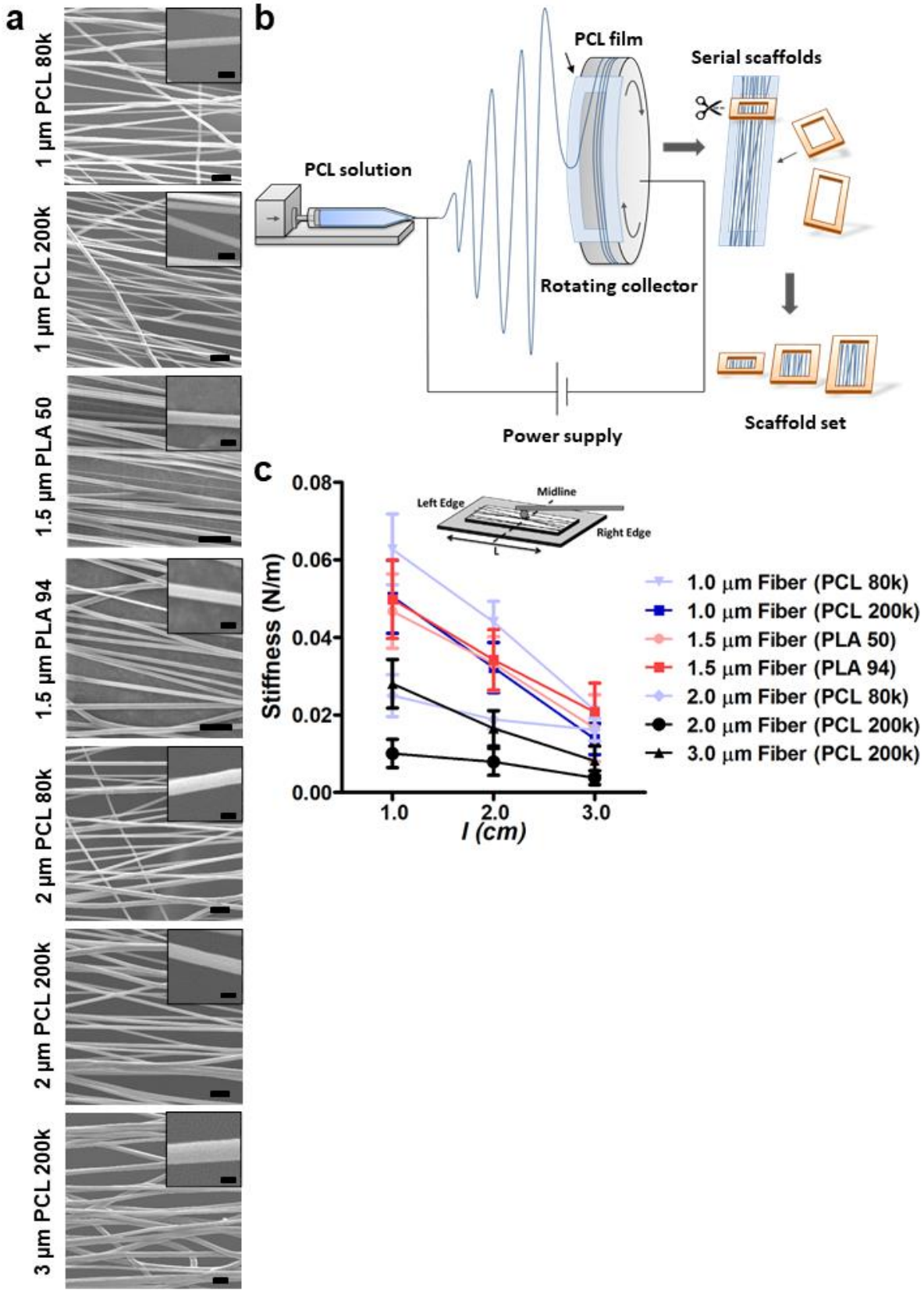
a
1 µm PCL 80k
1 µm PCL 200k
1.5 µm PLA 50
1.5 µm PLA 94
2 µm PCL 80k
2 µm PCL 200k
3 µm PCL 200k
b
PCL film
Serial scaffolds
PCL solution
Rotating collector
Power supply
Scaffold set
c
Left Edge
Midline
Right Edge
Stiffness (N/m)
0.08
0.06
0.04
0.02
0.00
1.0
2.0
3.0
l (cm)
1.0 µm Fiber (PCL 80k)
1.0 µm Fiber (PCL 200k)
1.5 µm Fiber (PLA 50)
1.5 µm Fiber (PLA 94)
2.0 µm Fiber (PCL 80k)
2.0 µm Fiber (PCL 200k)
3.0 µm Fiber (PCL 200k)

1

Supplementary Figure 2. Tunable structural stiffness platform engineered by changing length of support. **(a)** Scanning electron microscopy images of artificial axons engineered into suspended tunable stiffness platform with embedded images showing higher magnification. Scale bar of main image represents 10 µm, magnification 500X. Scale bar of embedded image represents 2 µm. **(b)** Illustration of engineering of tunable stiffness platform. Electrospun fibers were drawn from PCL solution onto a 50 µm thick, 8 cm long PCL film, which was mounted onto the collector. 0.5 mm thick PCL frames of various sizes were cut out by customized punchers and used to secure the fibers on PCL films with silicon glue. Individual scaffolds were cut and utilized for downstream experiments. **(c)** AFM measurements showing structural stiffness decreases with increasing length of support regardless of fiber diameter, materials and intrinsic stiffness. Thus, structural stiffness is decoupled from other physical parameters.

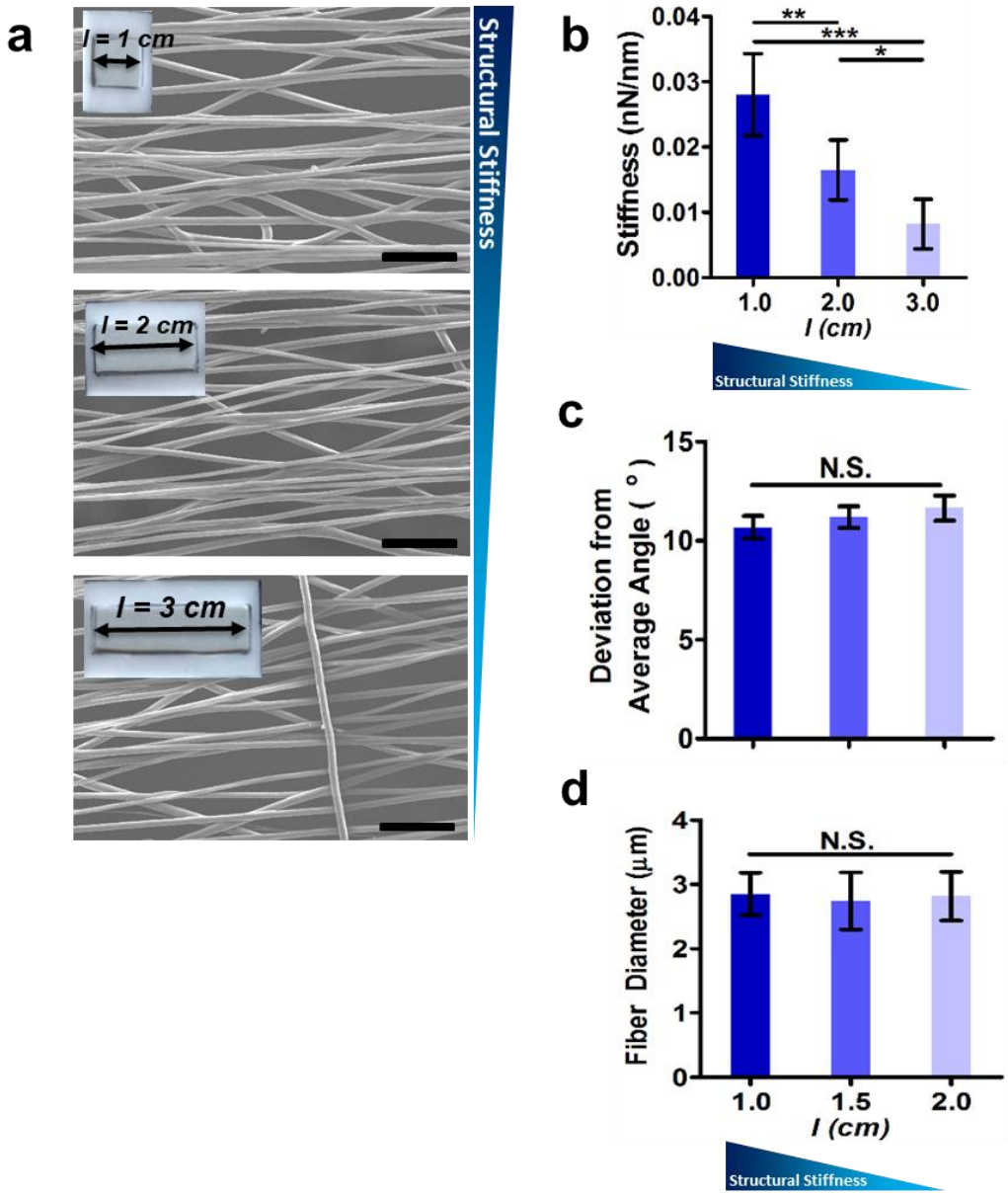

Supplementary Figure 3. Fabrication of artificial axons with tunable structural stiffness while keeping other physical parameters constant. (a) SEM images of artificial axons (diameter, ϕ: 3 μm, 200k M_n PCL) supported across different lengths of PCL frame (***l***). Scale bars represent 50 μm, magnification 500X. **(b-d)** Quantitative data showing decoupling of axon structural stiffness from other physical properties of artificial axons. **(b)** Axon structural stiffness decreases with increasing ***l*** (*p < 0.05, **p < 0.01, ***p < 0.001, One-way ANOVA with Tukey post-hoc), while maintaining similar **(c)** axon topography and **(d)** diameter. N.S. non-statistical significance, one-way ANOVA with Tukey post-hoc.

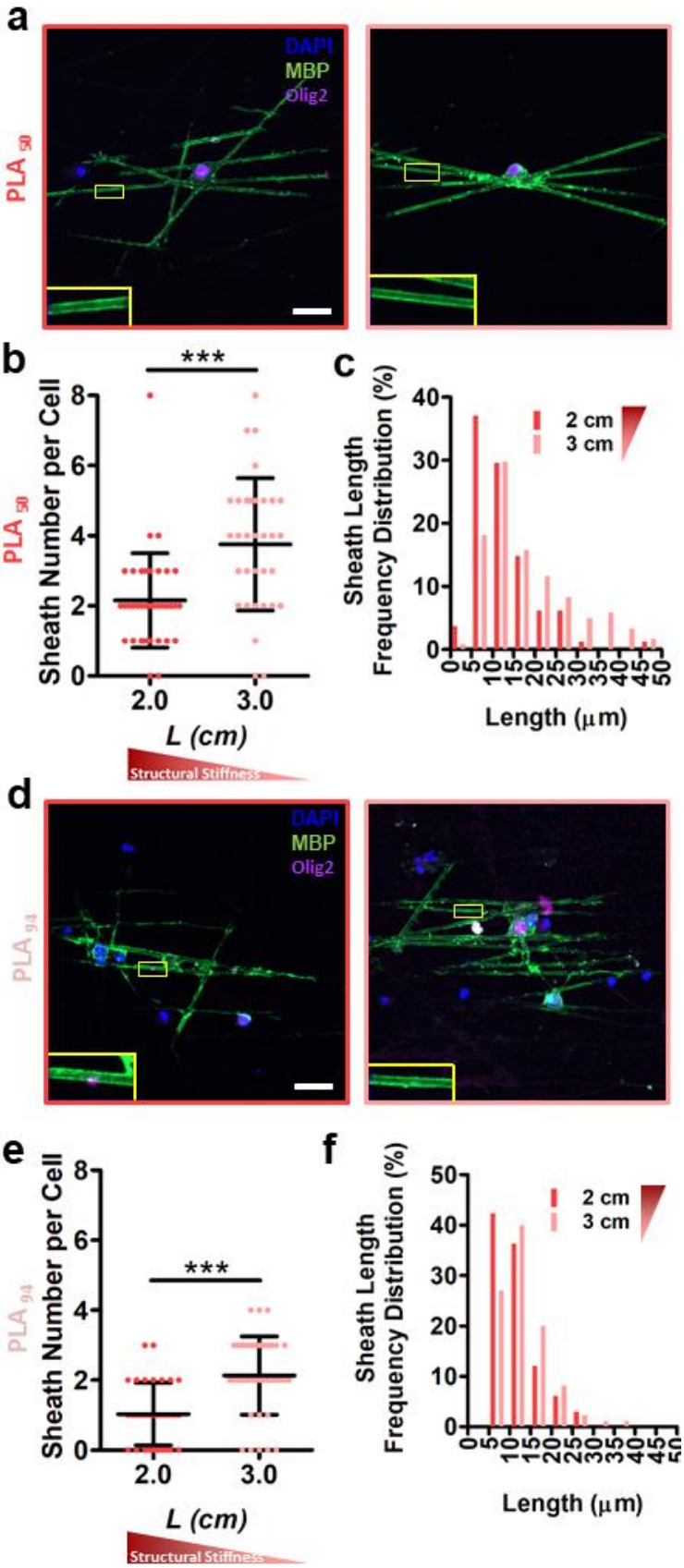
a
DAPI
MBP
Olig2
PLA 90
b
***
Sheath Number per Cell
PLA 90
2.0
3.0
L (cm)
Structural Stiffness
c
Sheath Length Frequency Distribution (%)
2 cm
3 cm
Length (μm)
d
DAPI
MBP
Olig2
PLA 94
e
***
Sheath Number per Cell
PLA 94
2.0
3.0
L (cm)
Structural Stiffness
f
Sheath Length Frequency Distribution (%)
2 cm
3 cm
Length (μm)

1

Supplementary Figure 4. OL myelination is impeded by increased structural stiffness of PLA artificial axons. (a) Representative confocal images show extent of OL myelination on PLA_{50} artificial axons. Scale bar represents 20 µm. **(b-c)** Quantitative data shows longer suspension length and thus, lower structural stiffness promote formation of more myelin sheath per cell and longer sheaths on PLA_{50} fibers. ***p<0.001, t-test. 71 cells pooled from 3 independent experiment and 9 animals. **(d)** Representative confocal images show extent of OL myelination on PLA_{94} artificial axons. Scale bar represents 20 µm. **(e-f)** Quantitative data shows longer suspension length and thus, lower structural stiffness promote formation of more myelin sheath per cell and similar myelin sheath length on PLA_{94} fibers. ***p<0.001, t-test. 70 cells pooled from 3 independent experiment and 9 animals.

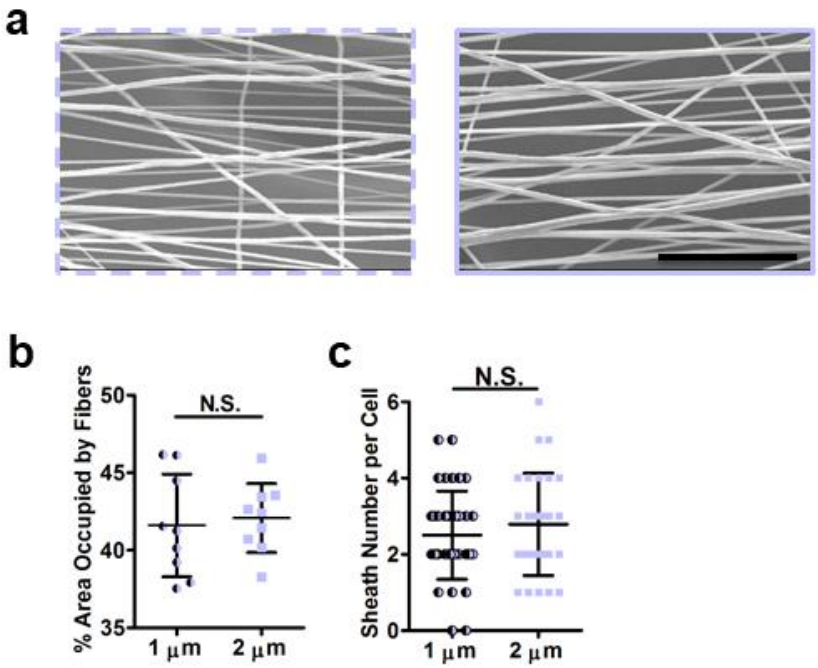

Supplementary Figure 5. OLs formed similar sheath number per cell when cultured on artificial axons with similar structural stiffness and fiber density. (a) SEM images showing electrospun PCL artificial axons with different diameter for OL myelination. Scale bar represents 50 µm. **(b)** Electrospinning parameter optimization enable similar fiber density to be achieved in suspended microfiber platform and thus maintaining the artificial axon demand of myelination. **(c)** Data showing higher artificial axon diameter formed similar number of myelin sheaths per cells. Non-statistically significant. Independent t-test. 66 cells pooled from 3 independent experiment and 9 animals.

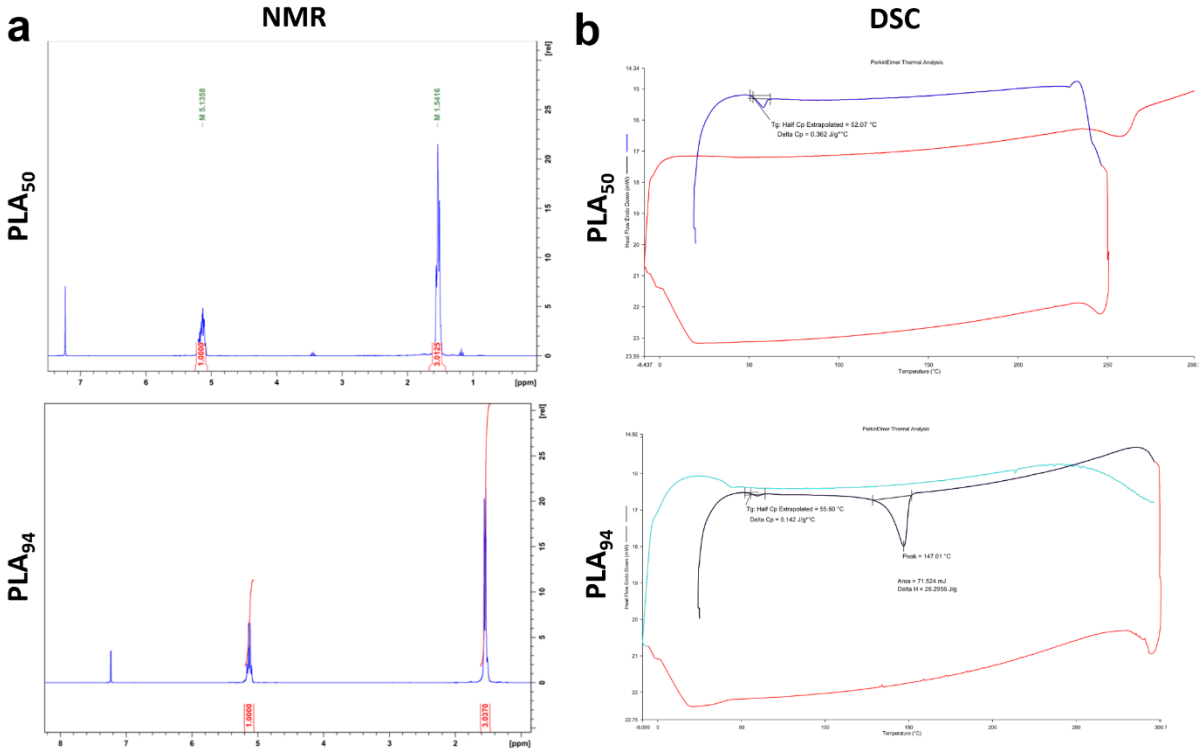

Supplementary Figure 6. Synthesis and characterization of PLA. (a) 1H NMR data shows the predicted PLA protons with ratio of 1:3 in both PLA_{50} and PLA_{94}. **(b)** Differential Scanning Calorimetry data showing polymers thermal properties values of PLA_{50} and PLA_{94}. PLA_{50} shows single glass transition peak that is correlated to amorphous structure while PLA_{94} shows an additional melting peak representing crystalline structure. Higher calorific capacity of PLA_{50} suggests large proportion of amorphous structure.

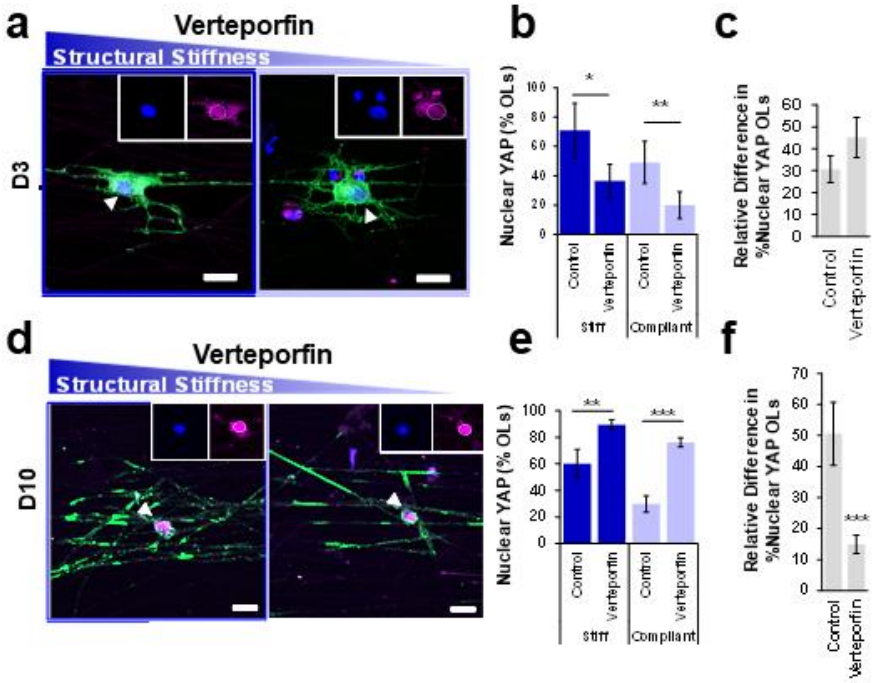

Supplementary Figure 7. Effect of verteporfin on YAP nuclear localization in immature OPCs and myelinating OLs. (a) Confocal images show cytoplasmic localization for YAP under verteporfin treatment (0.1 µM) at Day 3, for structurally stiff and compliant axons. Scale bar represent 20 µm. (b-c) Quantitative data show consistent inhibition of the YAP nuclear import by verteporfin throughout OPC differentiation, regardless of structural stiffness. *$p < 0.05$, ** $p < 0.01$, one-way ANOVA with Tukey post-hoc test. (d) Confocal images show nuclear localization for YAP under verteporfin treatment (0.1 µM) at Day 10, for structurally stiff and compliant axons. Scale bar represent 20 µm. (e-f) Quantitative data show consistent increase of the YAP nuclear import under verteporfin treatment for myelinating cells at Day 10, with a higher effect on cells on structurally compliant axons. ** $p < 0.01$, *** $p < 0.001$, one-way ANOVA with Tukey post-hoc test. (c) and (f) are showing the difference between the compliant and stiff axon relative to the stiff axon [(Compliant – Stiff) / Stiff x 100 %)]. All statistical analysis was conducted using n = 3 experimental (biological) repeats.

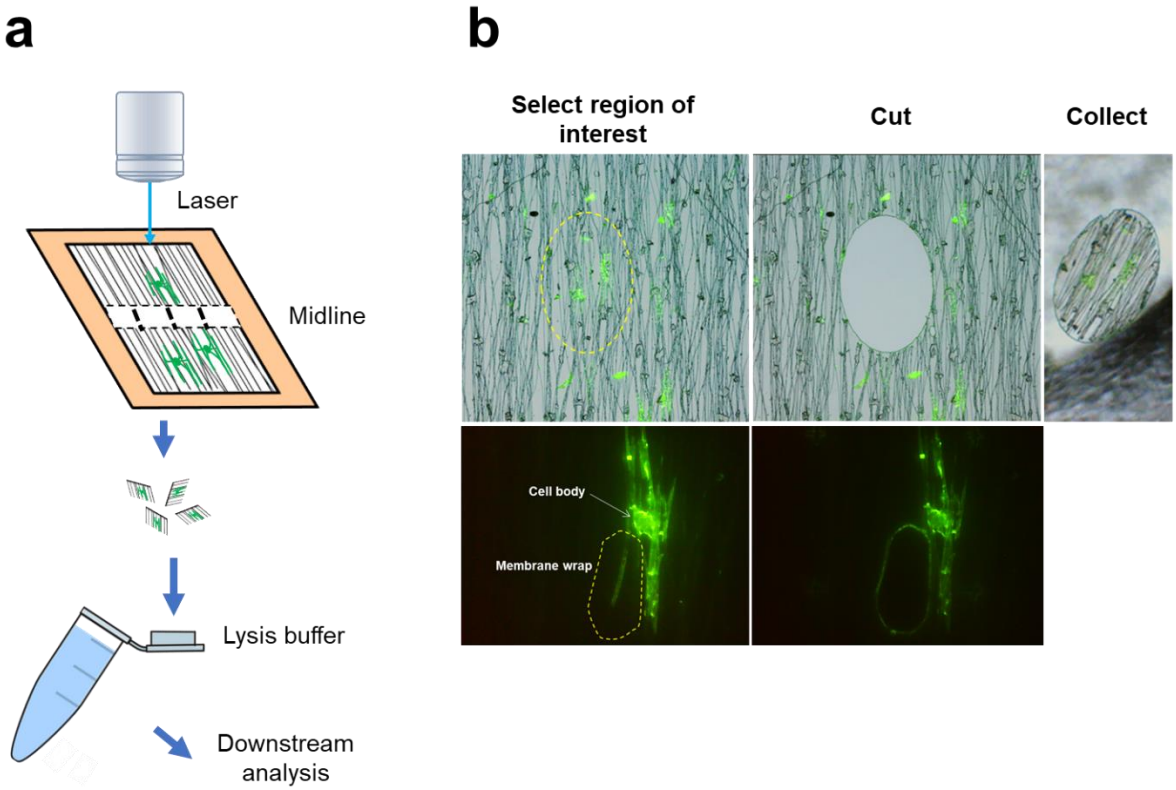

Supplementary Figure 8. Proof-of-principle of oligodendrocyte single-cell analysis with laser microdissection. (a) Drawing representing the principle of single-cell selective collection of myelinating cells along the scaffold midline through laser microdissection and the coupling with downstream analysis. **(b)** Microscopy images (magnification 10X) showing the selection and cutting of region of interest - myelinating cells or myelin sheath (MBP, green) - on microfibers (brightfield).